thesis for the degree of Licentiate of Engineering

Comb-based Characterization of Photonic Devices

Krishna Sundar Twayana

Photonics Laboratory
Department of Microtechnology and Nanoscience (MC2)
Chalmers University of Technology
Göteborg, Sweden, 2022

Comb-based Characterization of Photonic Devices
Krishna Sundar Twayana

ISSN 1652-0769
Technical Report MC2-453

Photonics Laboratory
Department of Microtechnology and Nanoscience (MC2)
Chalmers University of Technology
SE–412 96 Göteborg
Sweden
Telephone: +46 (0)76–219 58 50

Printed in Sweden by
Reproservice
Chalmers Tekniska Högskola
Göteborg, Sweden, 2022

Comb-based Characterization of Photonic Devices

Krishna Sundar Twayana
Photonics Laboratory
Department of Microtechnology and Nanoscience (MC2)
Chalmers University of Technology

Abstract

Integrated photonics has been one of the fastest-growing fields in science. Measuring photonic devices in amplitude and phase (i.e. complex response) provides insight into their performance. Swept-wavelength interferometry is a prominent technique for the broadband characterization of the complex response. It leverages continuous advances in rapidly tunable laser sources, but is prone to systematic errors associated to the calibration of the frequency.. This thesis focuses on the non-destructive characterization of ultralow-loss photonic devices using swept wavelength interferometric technique. We overcome issues associated to nonlinear tuning by calibrating the frequency of the laser with the aid of a frequency comb. We apply the concept to diverse components of relevance including microresonators and spiral waveguides. In addition, we provide an overview and comparative assessment of the state of the art in the field.

Keywords: frequency combs, microresonators, swept-wavelength interferometry, optical frequency domain spectroscopy, microcombs, waveguides, stepped-heterodyne technique

Publications

This thesis is based on the work contained in the following papers:

[A] K. Twayana, Z. Ye, Ó. B. Helgason, K. Vijayan, M. Karlsson, V. Torres-Company "Frequency-comb-calibrated swept-wavelength interferometry", *Optics Express*, **29**, 15, 24363-24372, 2021.

[B] K. Twayana, I. Rebolledo-Salgado, E. Deriushkina, J. Schröder, M. Karlsson, V. Torres-Company, "Spectral Interferometry with Frequency Combs", *Micromachines*, **13**, 4, 2072-666X, 2022.

[C] K. Twayana, F. Lei, Z. Ye, I. Rebolledo-Salgado, Ó. B. Helgason, M. Karlsson, V. Torres-Company, "Differential phase reconstruction of microcombs", *Submitted, 2022*

Contents

Acknowledgement

First, I would like to thank my supervisor, Professor Victor Torres-Company, for giving me the opportunity to study towards a PhD and for all of the support and supervision along the way. I am grateful to my co-supervisor and examiner Professor Magnus Karlsson for valuable support and guidance. I also thank Prof. Peter Andrekson for sharing helpful knowledge and insights.

I am thankful to all wonderful and brilliant people in the Photonics laboratory that I thoroughly enjoy discussing and working with. I am grateful to Dr. Attila Fülöp and Dr. Zhichao Ye for giving up so much of their time to teach me about simulation and device measurement in the lab. I would like to thank everyone at Ultra-fast photonics lab for cooperation and remarkable working ambience in the lab and office premises.

I would also like to acknowledge Horizon 2020 Framework Programme (GA 812818) and European Research Council (GA 771410) for financing my research and providing opportunities to participate in network conference and workshops with the partners institutes and industries.

Last but not least, I would like to thank all my friends and family for their incredible support throughout the years.

Acronyms

CEO	carrier envelope offset
CMOS	complementary metal–oxide–semiconductor
CMT	coupled mode theory
CW	continuous wave
DS	dissipative soliton
DKS	dissipative Kerr soliton
DOSPM	direct optical spectral phase measurement
DUT	device under test
ECDL	external cavity diode laser
EO	electro-optic
EOC	electro-optic comb
FROG	frequency-resolved optical grating
FSR	free spectral range
FWHM	full width at half maximum
FWM	four-wave mixing
GVD	group velocity dispersion
HNLF	highly non-linear fiber
IM	intensity modulator
LLE	Lugiato-Lefever equation
MI	modulation instability
Microcomb	microresonator frequency comb
MLL	mode-locked laser
MZI	Mach-Zehnder interferometer
NLSE	nonlinear Schrödinger equation
OCDR	optical coherence domain reflectometry
OFC	optical frequency comb
OFDR	optical frequency domain reflectometry
OLCR	optical low-coherence reflectometry
OPO	optical parametric oscillation

OTDR	optical time domain reflectometry
PM	phase modulator
RF	radio frequency
SNR	signal to noise ratio
SOI	silicon-on-insulator
SPIDER	spectral phase interferometry for direct electric-field reconstruction
SPM	self-phase modulation
SWI	swept-wavelength interferometry
TD	time domain
XPM	cross-phase modulation

Chapter 1

Introduction

Frequency is by far the quantity that can be measured with the greatest accuracy. The state of the art spectroscopy can measure a frequency with an accuracy of 20 decimal digits [1] using frequency rulers known as frequency combs. No other physical quantity can be measured with that level of precision. In order to make accurate measurements of physical quantities, a common strategy is to transduce them into frequency. Arthur Schawlow, the 1981 Nobel Prize winner in physics, advised to "never measure anything but frequency". In 1997, Theodore W. Hänsch had envisioned a self-referenced frequency comb for a universal optical frequency synthesis [2]. In the late 20^{th} century, an octave spanning of a fs pulse using a photonic crystal fiber and f-2f heterodyning enabled absolute frequency synthesis and metrology [3, 4]. For this contribution, John L. Hall and Theodore W. Hänsch were honored with half of the 2005 Nobel prize in physics. In the following years, a new research direction has immersed in the quest of rendering frequency combs on a microscale called 'microcombs'. Microcombs are generated in microresonators by employing the Kerr nonlinear effect from a CW pump laser. The nonlinear interactions give rise to the stimulated parametric mixing that leads to equidistant sidebands, which was first reported in [5]. Microcombs generated in the Si_3N_4 planar platform unravel the prospect of realizing frequency combs in highly compact, robust, and CMOS integration [6].

Integrated photonics has been one of the fastest-growing fields in science. The monolithic integration of silicon waveguides for optoelectronic devices had been demonstrated in 1986 [7]. However, the research in integrated silicon photonics gained momentum only from early 21^{st}. This acceleration was driven by power dissipation and bottleneck in data

transmission in data centers. Silicon photonics is one of the few areas in science ever to be adopted in the industry in less than a decade after its conception. In its early stage, an initial hindrance was seamless light propagation in and out of the integrated waveguide due to the fundamental discrepancy in the size of fiber and waveguide. This was dealt with delocalizing the light by tapering the waveguide [8] at coupling regions. For high-speed optical transmission, optical modulators are the key component. A silicon-based integrated modulator was proposed by carrier injection in [9], although it lacks the Pockels effect. The high index contrast of silicon on silicon-on-insulator (SOI) platform is ideally suited for the monolithic integration of a range of passive optical components.

The characterization of photonic devices is instrumental for the technological advancement and development of many applications. For example, in [10], measurement of wafer-level group and phase index is reported. This could assist in optimizing recipe growth in the subsequent deposition. In [11], relationship between roughness induced backscattering with optical parameters, polarization rotation, waveguide geometry, and higher-order mode coupled is illustrated. The characterization of photonic devices uses a laser as a probe and retrieves sensing information that is transduced in changes in amplitude and phase. This requires precise calibration of the laser. In general, the laser frequency is calibrated using auxiliary interferometry. However, this strategy is subject to subject to environmental perturbations and systematic errors attributed to the inherent dispersion. Laser frequency combs as an optical ruler are used for accurate frequency calibrate of tunable lasers [12].

1.1 This thesis

Measuring integrated photonic devices in amplitude and phase (i.e. complex response) provides insight into their performance. This thesis focuses primarily on the advanced characterization of ultralow-loss microresonators and waveguides. We set an external interferometric configuration of the sample for its non-destructive measurement. A self-referenced frequency comb was used as an optical ruler to calibrate the laser used in swept-wavelength interferometry and optical frequency domain reflectometry of the device under test (DUT). The characterization of photonic devices is instrumental for the use of these devices in various scientific applications. Frequency comb generation in microresonators is one application of interest in this thesis. This thesis also covers the

spectral and temporal characterization of microcombs, providing insight into the nonlinear dynamics of the waveforms with unprecedented sensitivity. This thesis covers the broadband differential phase measurement of microcombs whose repetition rate goes beyond the state of the art electronics bandwidth. It is based on a linear heterodyne technique assisted by electro-optic downconversion. Throughout the thesis, we used in-house fabricated Si_3N_4 samples to illustrate these new tools and methods.

Chapter 2 serves as a brief introduction to different types of frequency combs. Chapter 3 introduces the basic on swept-wavelength interferometry and self-referenced frequency comb calibration in tunable laser spectroscopy. It also highlights the specific applications in spectroscopy of the devices in detail. In chapter 4, analytical soliton comb dynamics in the microcavity are briefly discussed. The stepped-heterodyne technique is explained in detail and exemplified in the context of an EO-comb and microcomb. Finally, Chapter 5 provides the future outlook.

Chapter 2

Laser frequency combs

Frequency combs have unleashed enormous possibilities in science and technology. They provide a coherent and bidirectional link between optical and microwave frequencies. Earlier efforts to measure the laser frequency have based on harmonic frequency chains [13]. The rapid advance in mode-locked lasers as optical frequency comb generators eliminated the need for harmonic chains. Their basic principle are mode-locking by either an active element (optical modulator) or a nonlinear passive element (saturable absorber). In 1986, Ti-Sapphire as a broadband gain medium was introduced [14] enabling generation of a self mode-locked femtosecond laser [15]. The pulse train corresponds to a series of evenly spaced coherent frequency lines, called a 'frequency comb'. For optical frequency synthesis, the absolute position of the comb lines needs to be traced. In the late 1990s, John L. Hall and Theodor W. Hänsch came up with the revolutionary idea of using an octave-spanning comb and f-2f interferometry, enabling absolute frequency synthesis from radio-frequency atomic frequency references, which stand today as the basis for the SI unit of time. Mathematically, a frequency comb can be described as a train of pulses with an envelope function $A(t)$ modulating a carrier wave. The periodicity of the pulses is ensured by $A(t) = A(t - T)$ with $T = 1/f_r$ denoting the pulse repetition time. The electric field, however, is not periodic given that the carrier wave travels with its phase velocity. The electric field of the frequency comb can be represented according to [16]

$$E(t) = \mathrm{Re}(A(t)\mathrm{exp}^{-j\omega_c t}) = \mathrm{Re}\left(\sum_{n=-\infty}^{\infty} c_n \mathrm{exp}^{-j(\omega_c + n\omega_r)t}\right), \qquad (2.1)$$

with ω_c denoting the carrier frequency and c_n the Fourier series expansion coefficients of $A(t)$. Here, ω_c is not necessarily an integer multiple of ω_r. This causes a global offset (ω_{ceo}) of the modes. The offset is independent of the repetition rate. The frequency of the modes can then be reformulated as $\omega_n = n\omega_r + \omega_{ceo}$ considering $\omega_{ceo} < \omega_r$. In metrology, both the RF frequencies (ω_r and ω_{ceo}) have to be stabilized and referenced to create a frequency ruler. In the following, various types of frequency combs used in this thesis will be discussed briefly.

2.1 Optical frequency combs

Optical frequency combs are a workhorse in modern spectroscopy and metrology [17, 18]. The principle of frequency comb generation relies on mode locking developed in the mid-1960s after the invention of the laser. Mode locking generates a train of ultra-short optical pulses as a result of constructive interference between coherent lasing modes in the cavity. In the frequency domain, this results in an equidistant spectrum (comb lines) of repetition rate f_{rep} or f_r (used interchangeable in this thesis) as shown in Fig. 2.1. The frequency span of the comb is related to the inverse of pulse width. However, the pulse envelope and optical carrier wave walk-off introduces an offset frequency referred to the carrier envelope offset frequency (f_{ceo}). As such, the absolute frequency of the comb modes is represented as $f_n = nf_{rep} + f_{ceo}, n \in \mathbb{N}$. While f_{rep} is readily measured beating the comb lines, estimation of f_{ceo} usually requires a self-referencing i.e. octave-spanning comb. The limited bandwidth of the medium had prohibited such measurements until end of 1990s. The measurement of f_{ceo} was accomplished with broadening of mode-locked laser (MLL) via Kerr effect in a highly non-linear fiber (HNLF) and f-2f interferometry [3, 4]. The self-referenced frequency comb is a key for precise tuning laser frequency calibration and broadband spectroscopy of photonic devices which are discussed in chapter 3.

2.2 Electro-optic frequency combs

Electro-optic(EO) modulation is a technique for generating frequency combs. It is a combination of optical and microwave technology. To generate an EO-comb, a CW laser is modulated with an electro-optic modulator using an RF clock. Multiple sidebands are generated, centered around CW laser and spaced by the RF clock frequency. It is

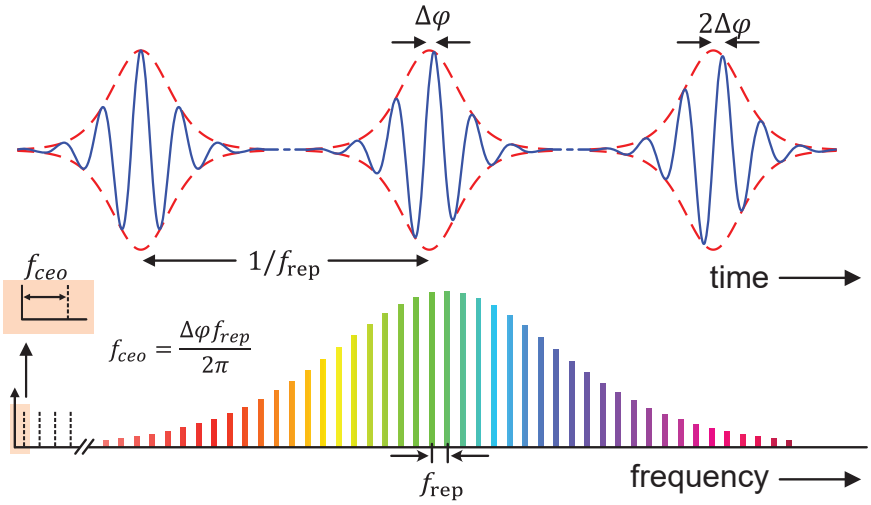

Figure 2.1: Temporal and spectral profile of a femtosecond optical frequency comb.

controllable, stable and a CW laser of any wavelength (compatible with the external modulator) is applicable as a light source [19].

Electro-optic (EO) combs are generated by electro-optic modulation of a continuous wave (CW) laser $C(t)$. The comb central frequency is defined by the seed laser and spacing by an RF clock. The key element in electro-optic modulation is a phase modulator (PM). The phase modulated electric field driven by an RF clock (modulating signal) can be modeled as

$$E_{EO}(t) = C(t)\exp^{j\beta\cos(2\pi f_r t)}, \tag{2.2}$$

with β denoting the modulation index and f_r the clock frequency. For simplicity, β can be expressed as normalized driving voltage $V_{rf}/V_\pi\pi$. Here, V_{rf} denotes the RF driving voltage and V_π half wave driving voltage for achieving a phase shift of π. The argument of equation 2.2 defines the frequency swing scaled by a carrier frequency with the maximum bandwidth $2\pi f_r V_{rf}/V_\pi$. The available RF power and practical V_π voltage limits the bandwidth range. The use of multiple PMs is in practice to extend the number of comb lines. It increases linearly with the number of cascaded modulators. The phase between the modulators can be aligned using RF phase shifters to change the shape of the comb spectrum.

The phase modulation in the sideband picture provides more insight on the comb spectrum. The phase modulation in terms of the n^{th} order

Bessel functions $J_n(\beta)$ is

$$E_{EO}(t) = |C(t)| \sum_{n=-\infty}^{\infty} J_n(\beta)\sin(2\pi(f_c + nf_r)t), \tag{2.3}$$

where $J_{-n}(\beta) = (-1)^n J_n(\beta)$ is the n^{th} order Bessel function of the first kind at modulation index β and f_c is the frequency of the seed laser. The phase modulation generates cascaded sidebands centered around f_c with the spacing f_r. As the sideband power is dependant on Bessel functions, it does not generate a flat spectrum. Therefore, an intensity modulator (IM) is sometimes used to flatten or equalize the amplitude of the comb-tones [20]. The IM based on a Mach-Zehnder interferometer driven by the RF signal $V(t) = V_{rf}\sin(2\pi f_r t)$ can be described according to the transfer function as

$$\frac{P_{out}}{P_{in}} = \frac{1}{2}\left[1 + \cos\left(\frac{\pi}{V_\pi}V(t) - \phi\right)\right], \tag{2.4}$$

The IM is biased at the center of the quasi-linear region. It carves out pulses when the chirp induced by the PM is quasi-linear generating a flat comb (Fig. 2.2(b)) [21]. The "rabbit ears" shape on each side of the flat region is attributed to the strong chirp at the edges. Figure 2.2 shows a schematic diagram, spectral, and temporal profiles of the EO-comb. The field envelope of the EO-comb comprises a train of pulses in the time-domain as shown in Fig. 2.2(c). The temporal phase profile takes the same profile as a modulating RF signal (Fig. 2.2(d)). A convex spectral parabolic phase profile (Fig. 2.2(e)) of the EO-comb suggests an anomalous dispersion. This phase relation between comb-tones indicates that the pulse is chirped and not transform-limited. A transform-limited (narrow train) pulse train can be restored by applying a reverse phase profile (dispersion value) using an appropriate dispersive component such as a waveshaper. Note that the phase profile can be opposite depending on the phase set by the phase shifter. In section 4.4.1, an EO-comb as a comb under test is used to illustrate the stepped-heterodyne technique.

2.3 Microcombs

Microresonator-based Kerr frequency combs ("microcombs") have attracted great attention as an optical source and witnessed significant research progress in the last decade [22, 23]. It is an active research area

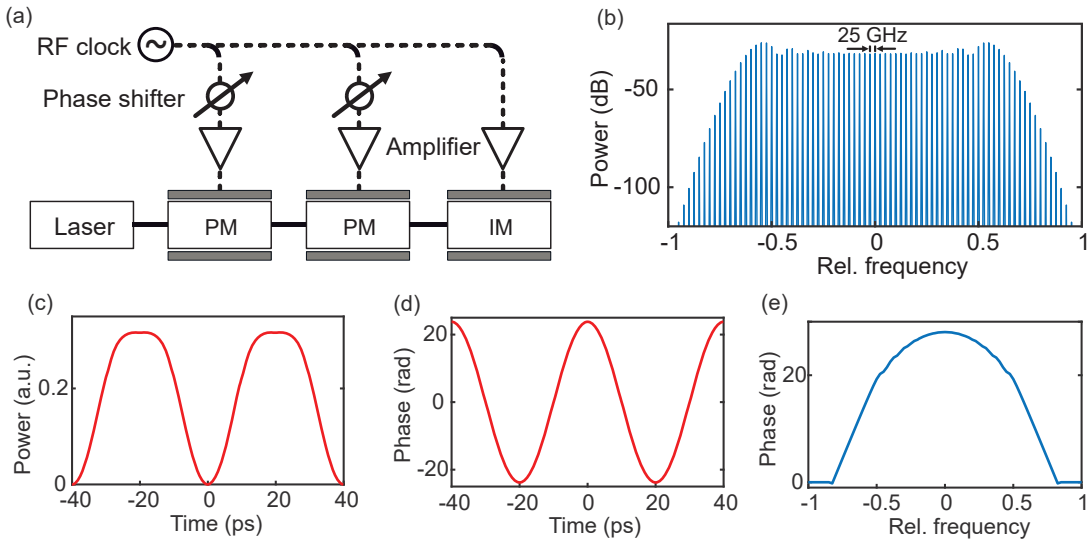

Figure 2.2: (a) EO comb generation setup consisting of two phase modulators and an intensity modulator. The cascaded PM increase the effective modulation depth and the IM flatten the output spectrum. Simulation of the EO comb for the setup in (a). (b) EO comb spectrum of $f_r = 25$ GHz. (c) Pulse profile of the EO comb with a period of $1/f_r = 40$ ps. (d) Phase in time-domain for modulation depth 11.5. (e) Parabolic phase distribution in frequency domain.

within chip-scale ultrafast optics and ultrastable lasers, enabling applications in spectroscopy [24] coherent communication [25, 26], optical clock generation [27], and optical frequency synthesis [28]. In 2004, optical parametric oscillation (OPO) in a Kerr microresonator was first demonstrated in a silica micro-toroid [29]. The idea of generating frequency combs in microresonators was proposed in [5] and stabilization relative to a microwave signal in [30]. The first demonstration of a microresonator frequency comb in an integrated platform was in silicon nitride (Si_3N_4) [6]. The frequency comb generation in a microcomb is initiated by parametric oscillation, followed by cascaded four-wave mixing processes [5]. This process is highly sensitive to the phase of the comb lines. This can lead to coherent waveforms such as dissipative solitons [31], which are self-enforcing optical pulses that circulate in the microcavity. In the spectral domain, the pulses coupled out of the cavity form a soliton microcomb with a fixed phase relationship between spectral lines similar to traditional mode-locked lasers. From knowledge of the comb lines' power and their relative phase, one can fully determine the temporal pulse shape of the microcomb [32] and synthesize the waveform by spatial modulation [33]. Comb dynamics in the microresonators are elaborated in chapter 4. Also, spectral and temporal features are illustrated

with simulations and measurements.

Chapter 3

Linear characterization techniques in photonic integration

3.1 Swept wavelength interferometry

Historically, the wave behaviour of light Young's double slit experiment and interferometry devised by Albert Michelson in 1890 are milestones in the advancement in the scientific understanding and development of optical technologies. In addition, the invention of the laser in the 1960s and tunable lasers in the following decades drove various interferometry techniques. TD (time doamin)-interferometry, spectral domain interferometry and swept-wavelength interferometry are various interferometry techniques. Optical reflectometry has been a long-standing nondestructive diagnostic tool to probe optical devices or for use in sensing applications. Basically, there are three reflectometric techniques: optical time domain reflectometry (OTDR), optical coherence domain reflectometry (OCDR), and optical frequency domain reflectometry (OFDR). All these techniques are in widespread use. Depending on the configurations and sources used, there are tradeoffs in terms of sensitivity, resolution, accuracy, speed, and range. OTDR allows measuring time resolved distributed reflection of short pulse and propagation losses [34]. It is used for long-distance over kilometers or more and low-resolution spectroscopy. OCDR also known as optical low-coherence reflectometry (OLCR) is essentially a multi-path interferometer using a low-coherence broadband source [35]. It uses a Michelson interferometer operated with

a broadband source when the time delay between the arms are nearly equal. It replaces one of the mirrors in the Michelson interferometer by the device under test. A translating mirror is scanned to locate fringes corresponding to reflection points within the DUT (device under test). OCDR with resolution of 10 μm and dynamic range of greater then 100 dB is demonstrated in [36]. In 1991, optical coherence tomography was first introduced to describe depth resolved biological imaging using the concept of OCDR [37]. This is time domain (TD-) OCT as envelope fringe pattern is acquired as a function of reference path delay to map reflectivity as a function of transverse plane position.

Swept-wavelength interferometry (SWI) has become a widespread high-precision measurement technique that is applied in a diverse array of applications. In the simplest case, it relies on an interferometric structure based on a broadband sweeping laser where one of the arms contains a device under test (DUT) (see Fig. 3.1). The laser source is swept across the measurement range in the interferometer and the signal is then detected by photodetectors. Interference fringe patterns are acquired as a function of time as the instantaneous frequency of the optical source is tuned. The Fourier transform of this pattern generates the complex impulse of the device under test (DUT). This allows a high resolution depth-resolved measurement, precise complex transfer function for metrology applications. The diverse array of utilities have been exploited in fiber optics [38], integrated photonics [39], tomography [40], and sensor systems [41].

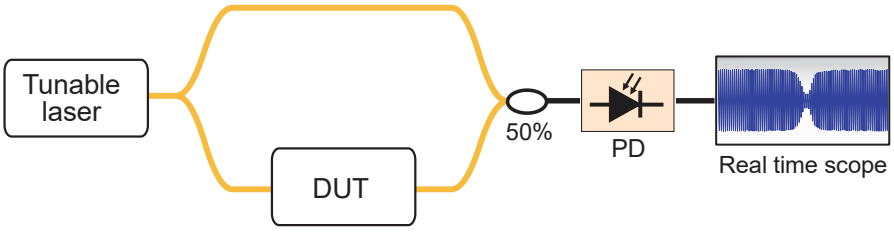

Figure 3.1: Typical Swept wavelength interferometry setup including a DUT.

Originally, optical SWI was aimed at measuring the reflection in optical fibers [42]. Being analogous to the widely adopted optical time domain reflectometry (OTDR) [43, 44], it was termed as optical frequency domain reflectometry (OFDR). In OTDR, distributed reflection is estimated by measuring the propagation delay of short pulses that are back-reflected by weak Rayleigh scattering in fibers. In contrast, OFDR is formed by coherent detection of the interference pattern between optical

signals from the test and reference paths when sweeping the laser. The measured beat frequencies can then be mapped into physical distances by knowing the speed of light in the medium.

The general expression of the co-polarized electric field from the arms having time delays τ_1 and τ_2 is expressed as

$$E_1(t) = (|E_1|e^{j\psi_1})e^{j2\pi(v_0+v\tau_1)t}, \quad E_2(t) = (|E_2|e^{j\psi_2})e^{j2\pi(v_0+v\tau_2)t}, \quad (3.1)$$

where E_i and ψ_i, $i \in 1, 2$ correspond to constant amplitudes and phases. For a linear tuning at a rate v, the instantaneous optical frequency at time t is $v_0 + vt$. The interference of these optical signals on a photodetector in turn generates a photocurrent given by

$$I(t) = I_0(1 + \cos(2\pi v\tau_0 t + \psi)), \quad (3.2)$$

where, $\tau_0 = \tau_1 - \tau_2$ and $\psi = \psi_1 - \psi_2$. This suggests that the delay can be inferred from the beating frequency given the linear tuning rate of the laser. However, the laser sweep is never linear in practice. Since the nonlinear tuning is ingrained in the argument of equation 3.2, it is difficult to disentangle from the relative phase difference of the DUT. Indeed, deviations from a purely linear wavelength sweep cause significant measurement errors and broaden the impulse response function [45]. This issue can be dealt with an active linearization of the tunable laser sources using the self-heterodyne interferometer [46, 47]. However, this technique is inconvenient and compatible only with some categories of tunable sources.

The interference pattern in equation 3.2 can be expressed as a function of instantaneous optical frequency as

$$I(\nu) = I_0(1 + cos(2\pi\nu\tau_0 + \zeta)), \quad (3.3)$$

with a trivial phase ζ. This expression assumes the instantaneous laser frequency does not vary rapidly over τ_0 [45]. The interference pattern is independent of the tuning rate in the frequency domain. In addition, the fringe pattern is periodic with a period $1/\tau_0$. This signal can be used as an external clock to sample an interferogram with a DUT arm of delay time τ_{DUT} [38, 48, 49]. This enables acquiring the fringe pattern free of non-linear laser tuning. However, it requires the Nyquist sampling criteria to be satisfied to avoid aliasing effects i.e. $\tau_{\mathrm{DUT}} \geq 2\tau_0$. Alternatively, an auxiliary interferometer can be used to calibrate the tuning of the laser frequency. The interference pattern is then mapped from the time

to frequency axis. However, these methods do not provide an absolute accuracy and also suffers from a systematic error. It requires the calibration of the auxiliary interferometer against the dispersion of the delay arm and operate in a stable condition [48, 50]. Thanks to the optical frequency ruler i.e. frequency comb, the frequency of tuning laser can be calibrated against this precise and accurate frequency markers. In the interferometric spectroscopes, frequency combs as a frequency ruler has been demonstrated for absolute distance measurement [51,52] and imaging [53]. The relevance of frequency comb in SWI for non-destructive characterization of ultra-low loss photonic devices is highlighted in Paper [A,B] and more detail is discussed in the following sections.

3.2 Frequency comb in tuning laser spectroscopy

The frequency comb as an optical ruler is an invaluable innovation that enables referencing an optical frequency with radio frequency accuracy. In [12], a self-referenced frequency comb was implemented for the spectroscopy of a tunable laser. The broadband precise calibration of the laser with sub-megahertz resolution enabled accurate dispersion measurement of microresonators. It is basically an interference between the laser with the comb pulse on a photodetector (Fig. 3.2). This in turn generates RF beatnotes from all the comb lines. The detection of the beat note associated with a particular comb line can be realized by using filters. A narrow bandpass microwave filter of central frequency f_{BP} generates a calibration marker when the scanning laser is $\pm f_{BP}$ away from the comb line. Therefore, the instantaneous laser frequency is calculated as $f_l = nf_{rep} + f_{ceo} \pm f_{BP}$. The sign of the $\pm f_{BP}$ term is related to the direction of the laser scanning. The narrow bandpass RF filters of center frequency f_{BP1} and f_{BP2} generate four beat markers per comb line as shown in Fig. 3.2. This allows a relative frequency calibration of the tuning laser. A reference laser with stable molecular absorption line can be used to resolve the frequency comb mode number (n) knowing the reference laser frequency with a relative accuracy better then half the f_{ref}. Furthermore, frequency combs allow calibrating cascaded lasers to extend the bandwidth range of spectroscopy while retaining absolute accuracy [54]. However, tuning of the laser in between the calibration markers is approximated by linear or by spline interpolation. The tuning of lasers can be traced more precisely with the aid of the Mach-Zehnder interferometer (MZI). We implemented this technique in the context of

swept wavelength interferometer (SWI) and exemplified it with characterizing low loss Si_3N_4 microresonators and spiral waveguides in papers [A and B].

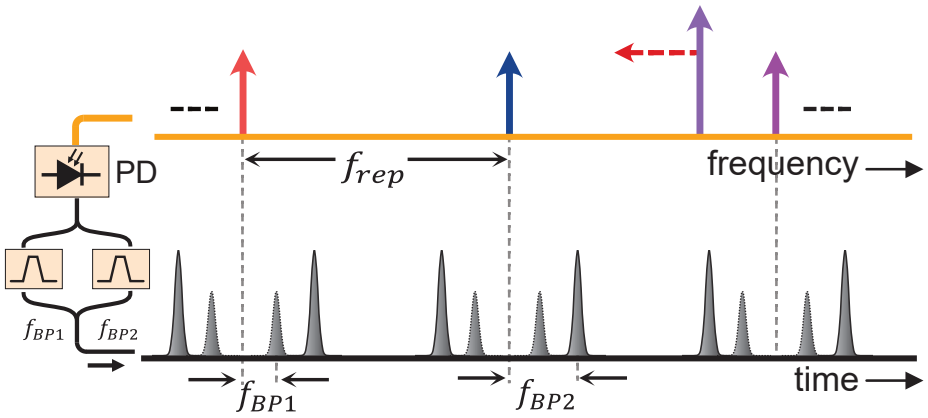

Figure 3.2: Self-referenced comb-assisted calibration of tunable lasers. Frequency comb and mode-hop free tuning laser (top), beat notes detected by two bandpass filters (bottom). The beatnotes are not necessarily equally spaced in time.

3.3 OFDR in waveguide spectroscopy

OFDR is a spectral domain reflectometry technique based on a fast sweeping laser source [55]. It fills the gap in measurement range between OCDR and OTDR. In addition, it provides higher SNR and spatial resolution. It is a spatially resolved highly-sensitive and non-destructive homodyne swept-wavelength interferometry technique. OFDR was initially motivated by the need to characterize distributed reflection in fibers for telecommunication applications [55]. With advances in technology, it has been exploited in characterization of fiber assemblies [38, 56, 57], integrated photonic devices [58–61], ranging systems [62], and biomedical imaging [40].

In OFDR, an auxiliary interferometer has been a long-established method to calibrate the nonlinear tuning of the laser. However, it is subject to external perturbations and systematic error introduced by inherent fiber dispersion. This results in broadening of the reflection peak and measurement deviation in features of the DUT. Instead of auxiliary interferometer, in [51, 52], OFDR absolute distance measurement was implemented using a frequency comb as a precise optical frequency

ruler. The used frequency comb is a free running mode-locked laser requiring sweeping laser to be tuned faster than CEO drift. In paper [A,B], we demonstrated the relevance of a self-referenced frequency comb for broadband precision in the phase measurement and propagation loss estimation of long spiral waveguides. This non-destructive analysis has helped the group improving the design and fabrication of the waveguides. Figure 3.3 illustrates the reflectivity profiles of the waveguide driven by fundamental quasi-TE and quasi-TM modes. The measured propagation loss is 4.23 dB/m for TE and 4.77 dB/m for TM mode. In both cases, there is a tiny reflection peak (shown by an arrow) along the waveguide segment, which indicates a fabrication defect. The defects were overcome in subsequent fabrications, resulting in world-record low loss of 1.4 dB/m [63, 64]. Fabrication of such an ultra-low loss meter long device calls for meticulous stitching error compensation as reported in [65]. The TE mode reflection peak in Fig. 3.3(b) is attributed to either the power coupling from the TM mode along the propagation or residual TE mode in fiber to waveguide power coupling.

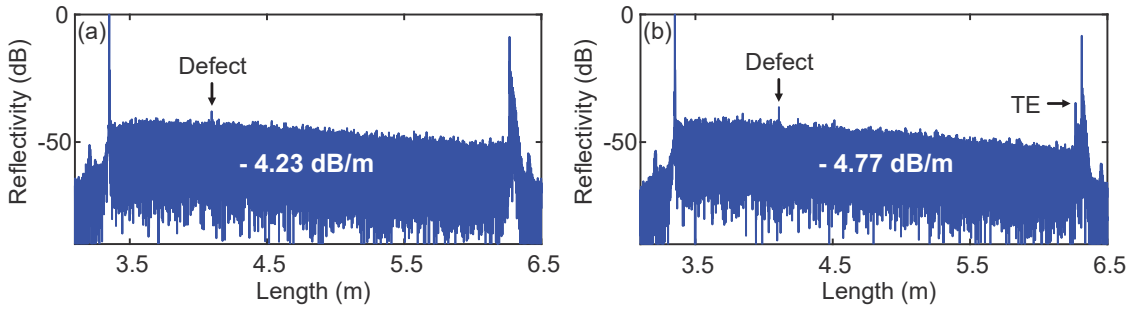

Figure 3.3: OFDR of the waveguide. (a) Spatial reflectivity of the fundamental quasi-TE mode. (b) Spatial reflectivity of fundamental quasi-TM mode.

3.4 Microresonator spectroscopy

Self referenced frequency combs for wavelength calibration of the laser is a prominent technique in a broadband high precision spectroscopy of microresonators [54]. It enables precisely resolving the frequency axis of the longitudinal modes and retrieving accurate dispersion values of different transverse mode families [12, 66]. The dispersion of microresonators results in relative offset of the resonances from the equidistant frequency grid. Other properties of the resonances (discuss below) are embedded in their profile [67]. As the resonance profile is invariant to

commutation of the coupling rate, the coupling condition cannot be distinguished [68]. In [69], the resonance condition is identified assuming weak wavelength dependent loss. It is possible to untangle the coupling condition by measuring also the phase responses of the resonances [67]. The resonance phase profile can be measured with a network analyzer by sweeping microwave modulation frequency [70]. However, the measurement range is restricted within the microwave sweeping range per scan. In [71], the phase profile of the resonances was extracted by fitting an interference pattern of a resonator coupled to a balanced MZI. In papers [A,B], we demonstrated the characterization of the microresonator configured in unbalanced MZI calibrated with self reference comb.

3.4.1 SWI of microresonators

In SWI, a microresonator is configured in one arms of a unbalanced interferometer. A mode-hope free tuning laser scans the interferometer and detect the sensing information transduces in the interference pattern. The amplitude transmission of the microresonator modulates the envelope and the phase response is encoded in the oscillations. The acquired interference pattern is mapped to the frequency axis with help of a fiber laser frequency comb. The Fourier transfer of frequency discretized interference pattern generates a impulse response of the device as shown in Fig. 3.4. The reference impulse (inset) is attributed to the interference of the probe signal without passing through resonator cavity. The inverse Fourier transform from those traces give the reference ($\mathcal{H}_{ref}$), and the overall ($\mathcal{H}_{tot}$) transfer function of the system. Therefore, the equivalent complex transfer function of the device under test is $\mathcal{H}_{ring} = \mathcal{H}_{tot}/\mathcal{H}_{ref}$. Figure 3.5 shows the normalized transmission and phase profile retrieved from the complex transfer function of the resonances. In Paper [A,B], we report SWI technique calibrated with self-referenced comb for broadband characterization in both amplitude and phase of the microresonator. In the following, we illustrate retrieval of other important properties of the resonances.

3.4.2 Parametric fitting of resonances

The smoothness of the resonance spectrum is limited by the spectral resolution and the overall noise in the system. As such, a parametric fitting is prevalent in extracting the properties of the resonances. The lineshape fitting model is applied to extract the properties of the resonances. The

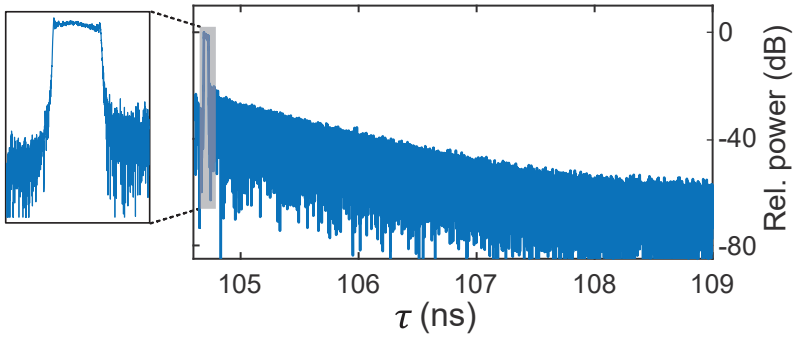

Figure 3.4: Impulse response of the SWI of the microresonator as a function of time delay. The microresonator properties are embedded in the inclining relative power trace. The zoom-in section is the reference impulse response of the SWI without the ring.

Lorentzian model is commonly used for the transmission spectrum fitting to retrieve the characteristic parameters of the resonances [72]. This fitting model allows unambiguous identification of the coupling parameter with the aid of the phase profile estimated as discussed above. The inverse Lorentzian lineshape of the resonance transmission spectrum is expressed as:

$$\mid \mathcal{H}_{ring}(\Delta f) \mid = 1 - T_{min} \frac{\Delta f_{\mathrm{FWHM}}^2}{4\Delta f^2 + \Delta f_{\mathrm{FWHM}}^2}, \tag{3.4}$$

where T_{min} is a normalized transmission at the resonance, Δf is a frequency detuning from the cavity resonance f_0 and Δf_{FWHM} is a full width half maximum (FWHM). The intrinsic Q-factor is calculated from the transmission spectrum as [72]:

$$Q_i = \frac{2Q_{tot}}{1 \pm \sqrt{T_{min}}}, \tag{3.5}$$

where the loaded Q-factor $Q_{tot} = \frac{f_0}{\Delta f_{\mathrm{FWHM}}}$ so that $\frac{1}{Q_{tot}} = \frac{1}{Q_i} + \frac{1}{Q_{ex}}$ is related to the total life-time of the photons in the cavity. It is composed of two loss contributions; photon decay rate due to waveguide coupling loss (extrinsic loss κ_{ex}) and the decay due to the scattering and absorption (intrinsic loss κ_i). In Eq. 3.5, the undercoupled resonance takes the $+$ sign and the overcoupled resonance takes the -sign. The intrinsic and extrinsic coupling rates are estimated as: $\kappa_i = f_0/Q_i$ and $\kappa_{ex} = f_0/Q_{ex}$ respectively. The Lorentzian lineshape fitting of some of the resonances are shown in the first row of Fig. 3.6.

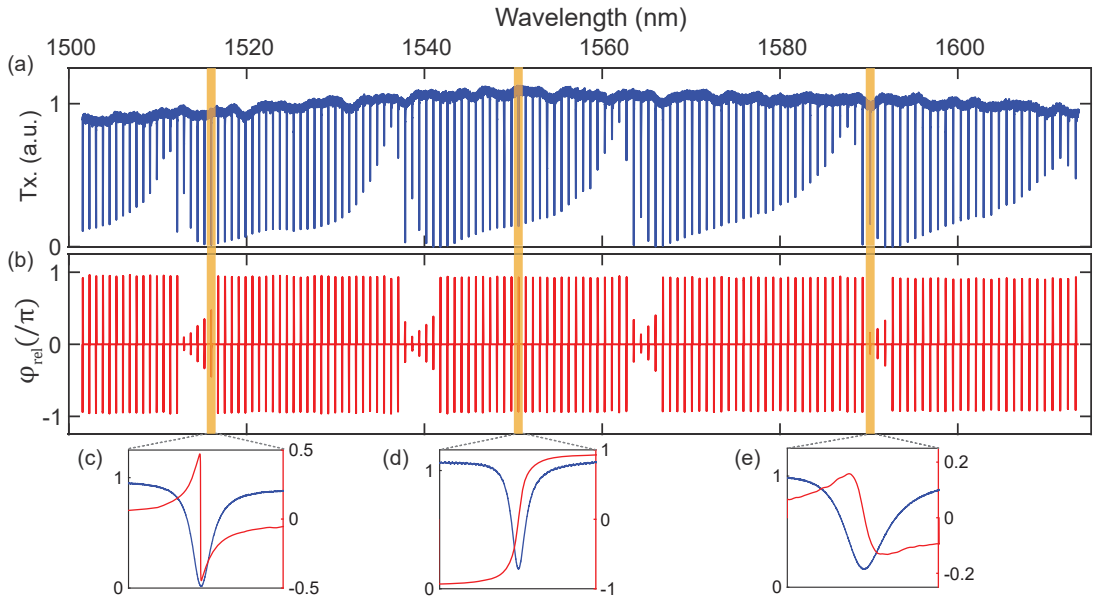

Figure 3.5: (a) Normalized transmission scan of a microresonator. (b) Linearized effective phase response of the resonator. Different coupling conditions: (c) Critical coupling. (d) Over-coupling. (e) Under-coupling.

In microresonators, distributed backscattering is inevitable due to the sidewall roughness. The coherent build-up of reflected light excites the counterclockwise (ccw) mode. The coupling between degenerate clockwise (cw) and ccw modes distorts the ideal Lorentzian profile and eventually leads to resonance-splitting [73]. In Fig. 3.6, the resonances feature no visible splitting, however, there is a noteworthy remnant of the counter propagating mode coupling. The Lorentzian fitting discussed above disregards this effect. Therefore, extended coupled-mode theory (CMT) in the time domain is widely adopted to retrieve the characteristics parameters of the resonances [74,75]. It is described by the following equations [76]

$$\frac{\partial E_+}{\partial t} = -(\frac{\kappa_i}{2} + \frac{\kappa_{ex}}{2} + i\Delta f)E_+ + iE_-\frac{\kappa_c}{2} + iE_{in}\sqrt{\kappa_{ex}}, \tag{3.6}$$

$$\frac{\partial E_-}{\partial t} = -(\frac{\kappa_i}{2} + \frac{\kappa_{ex}}{2} + i\Delta f)E_- + iE_+\frac{\kappa_c}{2}, \tag{3.7}$$

$$E_{out} = E_{in} + i\sqrt{\kappa_{ex}}E_+, \tag{3.8}$$

where E_+ and E_- are the complex field of the counter propagating modes, E_{in} is an input driving the clockwise mode, E_{out} is an output

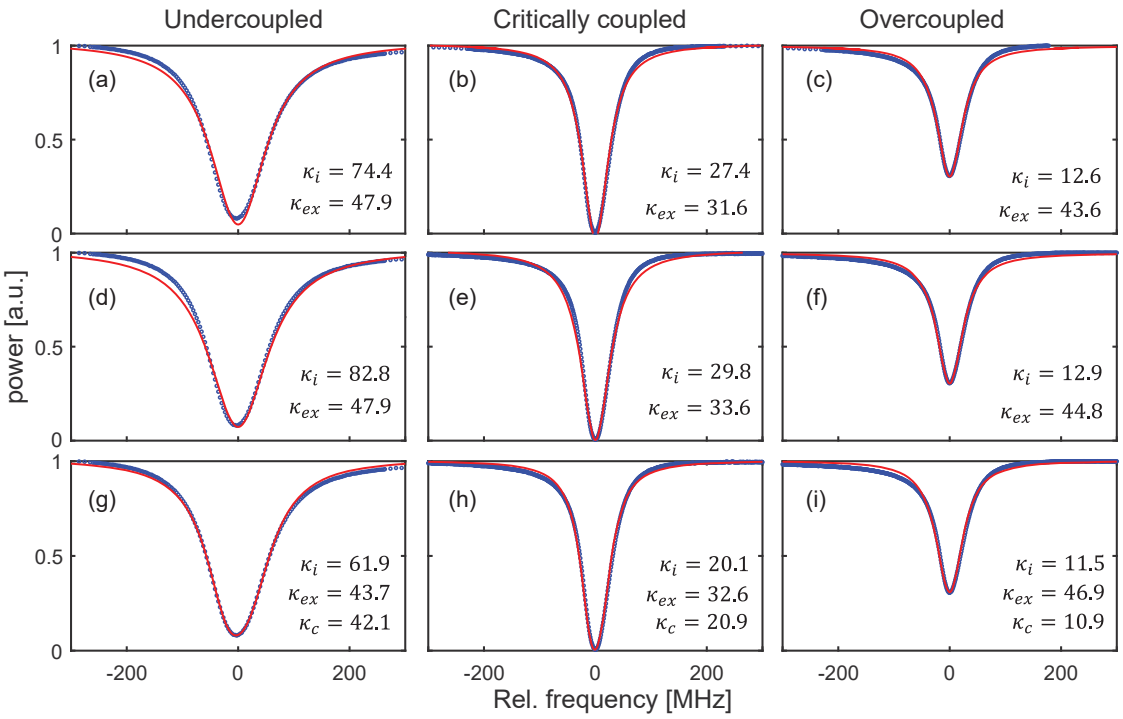

Figure 3.6: Normalized transmission spectra (blue) and parametric fitting profiles (red) of undercoupled, critically coupled, and overcoupled resonances in columns. The coupling rates have a unit of MHz. (a-c) Lorentzian lineshape fitting model. (d-f) Parametric coupled mode resonance fitting neglecting ccw mode coupling. (g-i) Parametric coupled mode resonance fitting considering ccw mode coupling.

field, κ_i is the intrinsic cavity rate, κ_{ex} is the external coupling rate, and κ_c is the complex coupling rate between clockwise and counterclockwise fields. The transfer function of the resonance spectrum is given by the steady state solution of coupled mode equations:

$$\mathcal{H}_{ring} = \frac{E_{out}}{E_{in}} = \frac{\kappa_i^2 - \kappa_{ex}^2 - 4\Delta f^2 + i4\kappa_i \Delta f + \kappa_c^2}{(\kappa_i + \kappa_{ex})^2 + \kappa_c^2 - 4\Delta f^2 + i4(\kappa_i + \kappa_{ex})\Delta f}. \tag{3.9}$$

When $\kappa_c = 0$, the resonance profile is equivalent to the Lorentzian distribution and the intensity transfer function becomes:

$$|\,\mathcal{H}_{ring}\,|^2 = \frac{(\kappa_i - \kappa_{ex})^2 + (2\Delta f)^2}{(\kappa_i + \kappa_{ex})^2 + (2\Delta f)^2}. \tag{3.10}$$

A parametric fitting of Eq. 3.10 allows direct retrieval of the κ_i and κ_{ex}. It is clear that these coupling rates are interchangeable. However, from the prior knowledge of the coupling condition the coupling rates are untangled as $\kappa_{ex} > \kappa_i$ for the overcoupled and $\kappa_{ex} < \kappa_i$ for the

undercoupled regime, respectively. Figure 3.6 shows that the Lorentzian fitting (first row) is in concurrence with the CMT fitting of the resonances for κ_c=0 (second row). The above fittings neglect the contribution of κ_c on the FWHM and attributes its implications on the κ_i and/or κ_{ex}. As such, it overestimates the net coupling rates or underrate the total Q-factor. Therefore, it is of utmost importance to consider κ_c in the parametric fitting.

In general, the CMT fitting considers a complex counter propagating mode coupling rate $\kappa_c = \kappa_{Re} + i\kappa_{Im}$. An asymmetric (symmetric) resonance is observed for complex (real) κ_c. The split mode resonance fitting of the resonances with the coupling strengths are shown in the third row of Fig. 3.6. The complex part of κ_c is not highlighted in the figure as the resonances are quite symmetric without a visible doublet. All the resonances fit well. Remarkably, resonance fitting and coupling rates in the third column of Fig. 3.6 are equivalent. This is due to the fact that the resonance has weaker κ_c. However, there is a significant disparity in the coupling rates when the κ_c is stronger (the first column in Fig. 3.6).

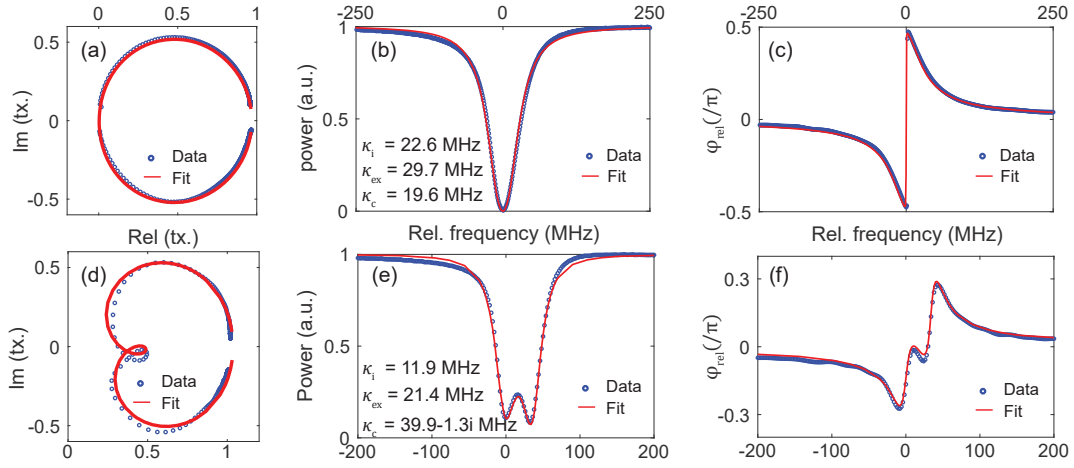

Figure 3.7: IQ plane fitting of the resonances. Critical coupled resonance (a) IQ plane plot, (b) resonance transmission profile, (c) Phase profile. Asymmetric split resonance (d) IQ plane plot, (e) resonance transmission profile, (f) Phase profile.

Paper [A], presents the first demonstration of empirical IQ plane parametric fitting of the resonances. Having an extra fitting dimension (phase), this fitting is more robust and returns an unambiguous and consistent set of coupling rates. The IQ plane parametric fitting of the single and split resonance field traces are illustrated in Fig. 3.7 (a)

and (d). The normalized resonance power and phase profile obtained from the complex plane fitting (red traces) are shown along with the corresponding measured profiles (blue traces). This fitting generates the coupling rates, in Fig. 3.7 (b) that absolutely satisfy the critical coupling condition i.e. $\kappa_c \sim \sqrt{\mid \kappa_{ex}^2 - \kappa_i^2 \mid}$. This is commensurate with the resonance transmission and phase profile. In Fig. 3.7(d), the inner loop is attributed to the resonance split. The resonance doublet with asymmetric resonance lineshape and the corresponding phase profile are shown in Fig. 3.7(e) and (f) respectively.

3.4.3 Loss measurement

Attenuation of a field strength propagating through a waveguide is attributed to inherent material absorption and Rayleigh scattering [11]. In addition, fabrication defects and inevitable side-wall roughness on the waveguide contribute to the losses. In integrated photonics, different techniques have been realized to estimate the propagation losses of waveguides [77, 78]. The cut-back method is the simplest way of evaluating the loss. It measures the insertion loss of several waveguides and extracts the propagation loss by calculating the slope versus waveguide length [79]. However, it relies upon uniformity of devices, facets consistency, and coupling accuracy. Another technique to measure the loss is OFDR, based on the distributed back-scattering of the light as discussed in section 3.3. This technique is independent of the facets reflectivity and fiber-waveguide coupling loss. The power difference of reflection peaks can also estimate the loss of the waveguide knowing the facets reflection coefficient [48]. However, OFDR assumes the loss is invariant in the propagation direction and constant over the spectral range of the scan. This technique is challenging to implement with the waveguide having shorter lengths. These limitations are overcome by using microresonators in the loss measurement. The loss is estimated from the finesse and extinction ratio at the resonances [80]. Also, intrinsic loss rate (κ_i) calculated from the parametric fitting can be used to estimation the loss. The equivalent propagation loss α per meter of the waveguide is calculated as [81]

$$\alpha \approx 2\pi \frac{\kappa_i}{L \times \mathrm{FSR}}, \tag{3.11}$$

where L is the round trip length and FSR is the free spectral range. This loss α per meter is expressed in dB per meter as $\frac{\log(10)}{10} \times \alpha$. Figure 3.8 shows the measured propagation loss of the microresonator with

an average value 3.08 dB/m. This variation of loss is attributed to the wavelength dependent transversal mode coupling and N-H bond absorption. This method assumes lossless coupling between the waveguide and resonator [82]. The measured loss also includes contribution from bend associated loss mechanism.

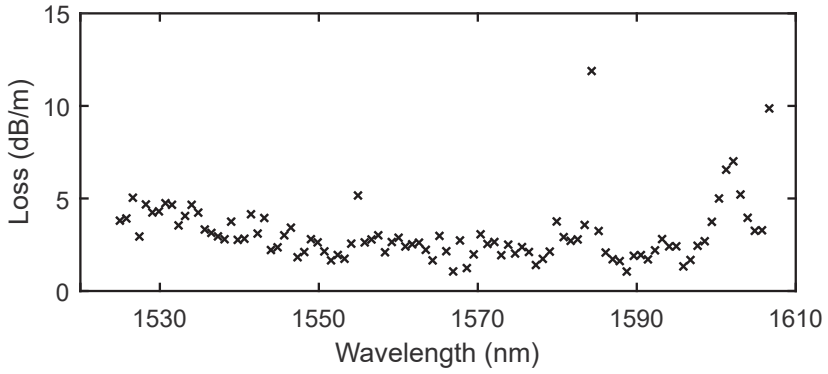

Figure 3.8: Measurement of the broadband propagation loss of a microresonator.

3.4.4 Dispersion in microresonators

The measurement of optical properties discussed above is highly dependent on the resonance lineshape. A small relative frequency offset of the resonances will not impact the extraction of the resonance properties. Therefore, absolute accuracy is not that critical for extracting those parameters. For our high-Q microresonators, the resonance linewidth is below 50 MHz. It is fairly reasonable to assume a constant group delay of fiber for such a narrow linewidth range. This brings to us the idea of using a traditional auxiliary interferometry technique in laser frequency calibration. We verified that the extraction of the resonance properties using auxiliary interferometry matches well with the frequency comb calibration technique. In contrast, the relative frequency offset of the resonance frequency due to the systematic error (frequency dependent group delay) of the auxiliary interferometer causes signification deviation in dispersion measurement of microresonators. Therefore, the precise frequency calibration of the tuning laser is of interest in the dispersion measurement. The frequency comb assisted laser frequency calibration is highly relevant in this context. Dispersion measurement also demands a high spectral resolution as the linewidths and the mode spacing deviations are in the order of kHz and MHz. The spectral resolution depends

on the bandwidth scanning range and the memory depth of the acquisition system.

In microresonators, resonance occurs if the phase shift of field after one roundtrip is an integer multiple of 2π, i.e. $\beta(\omega_\mu) - \beta(\omega_0) = 2\pi\mu/L$; $\mu \in \mathbb{Z}$. Here, ω_0 is the reference resonance frequency and ω_μ is the μ^{th} resonance count from the ω_0. This resonance condition under the Taylor expansion of the frequency dependent propagation vector β is

$$(\omega_\mu - \omega_0)\beta_1(\omega_0) + \frac{(\omega_\mu - \omega_0)^2}{2}\beta_2(\omega_0) + \frac{(\omega_\mu - \omega_0)^3}{6}\beta_3(\omega_0) + ... = \frac{2\pi\mu}{L}, \tag{3.12}$$

where β_0 is the phase velocity, β_1 is the group velocity, and β_2, β_3,... are dispersive orders. The dispersion parameters are extracted by a polynomial fit for all the resonances with respect to the reference resonance ω_0. The dispersive orders are related to the Taylor expansion of the propagation constant $\beta(\omega)$ with frequency:

$$\beta_2(\omega) = \beta_2(\omega_0) + \beta_3(\omega_0)(\omega - \omega_0) + \frac{\beta_4(\omega_0)(\omega - \omega_0)^2}{2} + ..., \tag{3.13}$$

Figure 3.9(b) shows the measured GVD at the resonance frequencies for a microresonator directly calculated from the Eq. 3.13.

In microresonators, the dispersion can also be described as the variation of FSR over resonance frequencies as in equation 3.14. This is a common metric of describing spectral extension and shape of microresonator frequency combs. Due to the higher order dispersion acts upon the GVD, dispersive waves induce at $D_{int} = 0$. This is a key feature of generating an octave spanning comb in microresonators [83, 84].

$$\omega_\mu = \omega_0 + \sum_{j=1} \frac{D_j \mu^j}{j!} = \omega_0 + D_1\mu + \frac{1}{2!}D_2\mu^2 + ... = \omega_0 + D_1\mu + D_{int}, \tag{3.14}$$

where, ω_μ is the μ^{th} order resonance frequency relative to ω_0. $D_1/2\pi$ corresponds to a mean FSR and D_{int} is a deviation of the resonance frequency from an equidistant resonance grid attributed to all dispersive terms ($D_2/2\pi, D_3/2\pi, ...$ in Hz). These coefficients are mutually related to the coefficients in equation 3.12 as $\beta(\omega_0 + \sum_{j=1} \frac{D_j\mu^j}{j!}) - \beta(\omega_0) = 2\pi\mu/L$. It can be established by Taylor expansion about ω_0 and equating the coefficients of μ^j, that results:

$$\beta_1 = \frac{2\pi}{D_1 L}, \qquad \beta_2 = -\frac{2\pi}{L}\frac{D_2}{D_1^3}, \qquad \beta_3 = -\frac{2\pi}{L}\frac{D_3}{D_1^4}, ..., \tag{3.15}$$

Figure 3.9(a) is the integrated dispersion (D_{int}) plot of the microresonator for the reference mode at 1565 nm with the FSR $D_1/2\pi = 105.2$ GHz. There are weak mode crossing effects clearly visible at some resonance frequencies. The convex parabolic feature of the D_{int} plot suggests a normal dispersion of the microresonator. $D_2/2\pi$ denotes the difference in FSR for adjacent modes. With 10 ps^2/km accuracy in the β_2 calculation, one need $\sim 2\pi \times 90$ kHz resolution in the $D_2/2\pi$ for $D_1/2\pi = 2\pi \times 100$ GHz and radius 227 μm. In broadband spectroscopy, resolution accuracy in sub-mega hertz is impractical because of limited data points per trace of the oscilloscope and uncertainty in the laser calibration introduced by the RF detection unit. However, β_2 is measured with increased accuracy averaging $D_2/2\pi$ over a larger set of the resonances. The average extracted $D_2/2\pi \sim -730$ kHz corresponds to $\beta_2 = 73$ ps^2/km at 1565 nm. It requires a separate polynomial fitting to estimate β_2 at a different resonance frequency.

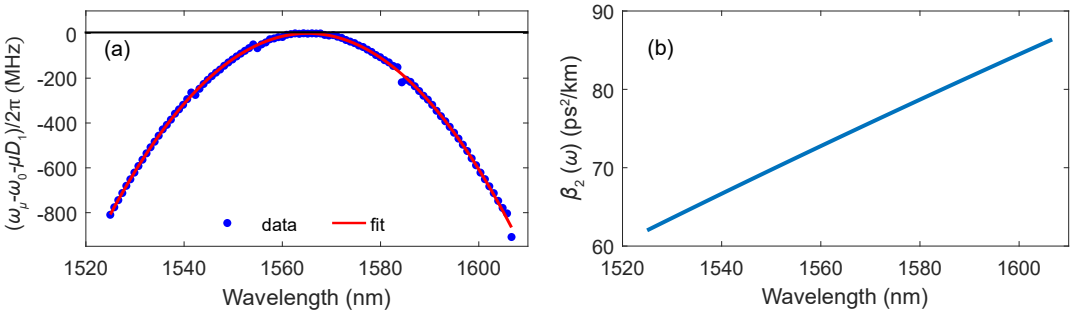

Figure 3.9: (a) Deviation of the resonance frequencies (D_{int}) from an equidistant frequency grid $\omega_0 + D_1\mu$ (gray line), where the reference mode is at 1565 nm. (b) Second order dispersion plot of the microresonator.

Chapter 4

Characterization techniques of microcombs

Microcombs are based on the Kerr nonlinear effect of four-wave mixing (FWM) processes. In particular, degenerate FWM processes generate a signal photon (ω_s) and an idler (ω_i) photon from two pump photons (ω_p). The conservation of energy ($2\omega_p = \omega_s + \omega_r$) ensures new equidistant frequency pairs. However, the coherence properties of microcombs were not known until Ferdous et al. demonstrated the microcomb phase measurement [85]. The phase measurement of the microcombs is crucial but challenging to implement. It provides physicists to investigate the comb dynamics, coherence of the spectrum, and ultra-short pulse in the cavity. In the following, we discuss dynamics of field propagation in nonlinear media and the formation of soliton combs. Then we talk about linear stepped-heterodyne technique comb characterization and exemplify it in the context of an EO-comb and microcomb.

4.1 Optical field propagating in a nonlinear medium

The wave optics model governed by Maxwell's equations describes the field distribution in the waveguide. According to wave optics, waveguides support only finite eigenmodes with a specific wave vector [86]. In the propagation of the field, it is prominent to consider the Kerr effect (discovered by John Kerr in 1875) due to the nonlinear interaction of light. It represents an effect of intensity dependent refractive index in the medium. Pulse propagation in a single-mode nonlinear medium

is then well described by the nonlinear Schrödinger equation (NLSE) according to [87]

$$\frac{\partial A}{\partial z} = \left(-\frac{1}{2}\alpha + i\sum_{n\geq 2} \frac{\beta_n}{n!}\left(i\frac{\partial}{\partial t}\right)^n + i\gamma|A|^2 \right) A, \tag{4.1}$$

where A is the slowly varying field envelope guided along the waveguide (z-axis). The propagation loss per unit length is α while β_n denotes the coefficients of the Taylor expansion of the propagation constant. The nonlinear parameter γ is a function of susceptibility $\chi^{(3)}$ and the effective mode area. Nonlinear effects such as self-phase modulation (SPM), cross-phase modulation (XPM) and four-wave mixing (FWM) are given by the γ parameter. This nonlinear differential equation is challenging to solve analytically. Therefore numerical simulations using the split-step Fourier method are widely adopted to understand the field propagation dynamics [87].

In a cavity, the field propagation dynamics consider the evolution of a slowly-varying field over consecutive round trips. It can be described in two sequential steps for each round trip (known as the Ikeda map) [88]. In the cavity, the field evolves under the influence of propagation loss, dispersion, and Kerr nonlinearity according to equation 4.1. At a coupling region, there is an exchange of optical power described as

$$A^m(0,t) = \sqrt{\theta}A_{in} + \sqrt{1-\theta}A^{(m-1)}(L,t)e^{j\delta_0}, \tag{4.2}$$

with θ denoting the power coupling coefficient, A_{in} driving field, A^m m^{th} ($m \in \mathbb{N}$) roundtrip field, and L is the cavity length. The parameter δ_0 represents a relative phase drift of the wave compared to the phase of closest resonance ($\delta_0 = \Delta\omega/\text{FSR}$). This is often called the detuning parameter and is applied at the end of each roundtrip. The Ikeda map model is widely used to simulate the evolution of pulses in microresonators.

4.2 CW pump to microcomb generation

The Ikeda map model can be simplified into a single equation known as the Lugiato-Lefever equation (LLE) [89]. The LLE provides an analytical understanding of the initialization and the dynamics of microcombs. The derivation of the LLE assumes negligible field changes over a single

roundtrip i.e. $A^{m-1}(L,t) = A^{m-1}(0,t) + L\frac{\partial A}{\partial z}$. With an approximation of a weak coupling and small detuning equation 4.2 turns out to be

$$A^m(0,t) \approx \sqrt{\theta}A_{in} + A^{(m-1)}(0,t)(1-\theta/2+i\delta_0) + L\frac{\partial A}{\partial z}, \tag{4.3}$$

Applying the equations 4.3 and 4.1 on a slow time evolution of the wave $\frac{A^m(0,t)-A^{m-1}(0,t)}{t_r}$ over a roundtrip time (t_r) leads to the LLE equation

$$t_r\frac{\partial A}{\partial \tau} = \left[-\sigma - i\delta_0 + iL\sum_{n\geq 2}\frac{\beta_n}{n!}\left(i\frac{\partial}{\partial t}\right)^n + i\gamma L|A|^2\right]A + \sqrt{\theta}A_{in}, \tag{4.4}$$

where $\sigma = (\alpha L+\theta)/2$ denotes the total cavity losses in a single roundtrip and τ is the slow time.

The LLE can describe the steady state behaviours of the microcombs driven by the CW field. All the time dependent functions are dropped from the LLE to get the steady-state solution (below) of the field envelope circulating in the cavity.

$$(-\sigma - i\delta_0 + i\gamma L|A|^2)A = -\sqrt{\theta}A_{in}, \tag{4.5}$$

This is a complex third-order polynomial equation in A. To simplify the solution, we multiply both sides with their conjugate:

$$\theta|A_{in}|^2 = (\sigma^2+\delta_0^2)P - 2\gamma L\delta_0 P^2 + \gamma^2L^2P^3, \tag{4.6}$$

Here $P = |A|^2$ is the intracavity power. Figure 4.1 shows the steady state solutions as a function of the detuning parameter. It is worth noting that stable solutions are the minimum and maximum power of the bistability region. The analytical steady state solution of the LLE for a non dissipative cavity turns out to be a soliton pulse $A_s(t)$ [31]. The intensity and phase profile of the intracavity pulse is shown in Fig 4.2.

$$A_s(t) = \sqrt{\frac{2\delta_0}{\gamma L}}\text{sech}\left(t\sqrt{\frac{2\delta_0}{\mid\beta_2\mid L}}\right), \tag{4.7}$$

While the bistability analysis only considered the CW solution, the presence of perturbations excite modulation instability (MI). This is a form of parametric amplification that initializes the comb generation processes in the cavity from weak modulations on the the CW pump,

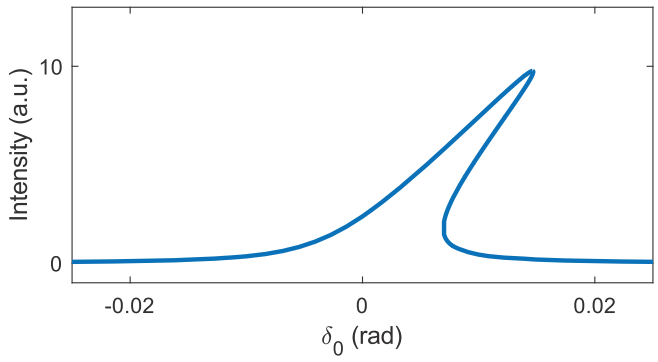

Figure 4.1: Bistability curve showing the intracavity power as a function of the detuning. The parameters are as follows: $\beta_2 = -65$ ps^2/km, $\gamma = 1.09\text{W}^{-1}\text{m}^{-1}$, $n_g = 2$, FSR=100 GHz.

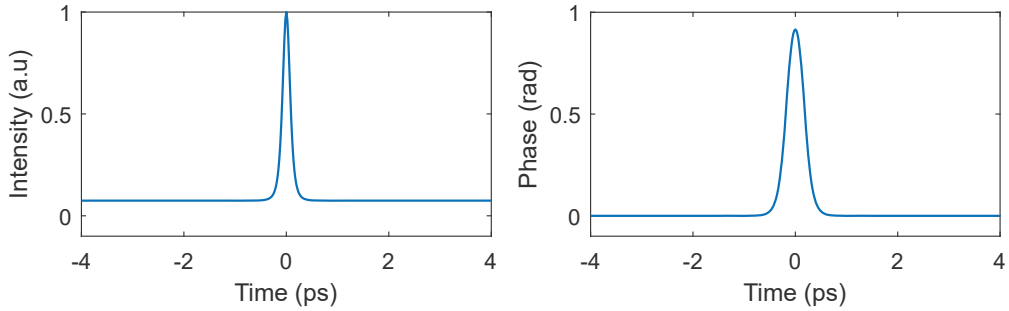

Figure 4.2: Temporal soliton pulse (a) and phase profile (b). The parameters are as follows: $\beta_2 = -65$ ps^2/km, $\delta_0 = 0.006$ rad, $\gamma = 1.09\text{W}^{-1}\text{m}^{-1}$, $n_g = 2$, FSR=100 GHz.

that are unstable and grow exponentially [87]. From the LLE, a gain coefficient profile for MI can be derived by applying a small perturbation in the field envelope. The normalized gain at a frequency offset $\Delta\Omega$ from the pump is [90]

$$G(\Delta\Omega) = \sqrt{(\gamma LP)^2 - (\delta_0 - 2\gamma LP - L\beta_2\Delta\Omega^2/2)^2},. \tag{4.8}$$

Note that the term under the square root is positive and overcomes both the propagation and coupling losses. In this equation, higher-order even dispersive terms are neglected. Figure 4.3 shows the MI gain along with the resonance spectrum. The gain spectra initialized by MI and pump experience cascaded four wave mixing (FWM) processes leading to equidistant comb lines. For equation 4.8, the maximum MI gain at a certain $\Delta\Omega$ requires

$$\Delta\Omega^2 = 2\frac{\delta_0 - 2\gamma LP}{\beta_2 L}, \tag{4.9}$$

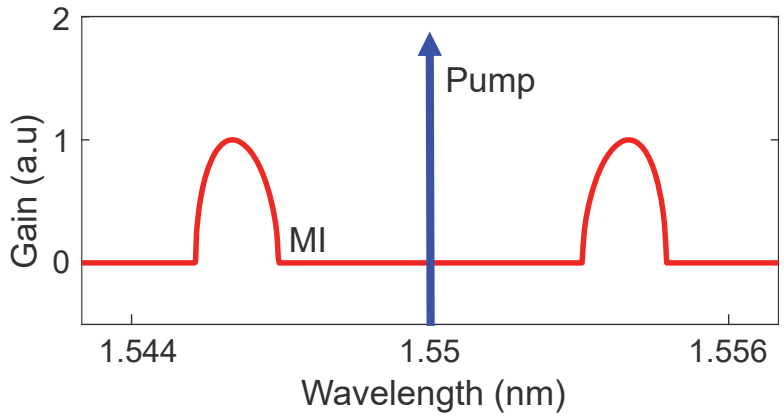

Figure 4.3: MI gain spectrum (red) with the CW pump (blue) plot.

This is a phase-matching condition for the MI gain. It suggests that the MI is accessible in the anomalous GVD ($\beta_2 < 0$) for $\delta_0 < 2\gamma LP$. This is a regime where the dissipative Kerr soliton (DKS) comb is generated. In paper D, we used a microresonator of anomalous GVD to generate dissipative single and multiple soliton combs. In the normal GVD regime($\beta_2 > 0$), MI requires $\delta_0 > 2\gamma LP$. However, the resonance detuning can be engineered and induce a localized anomalous GVD. This is enabled by the idea of mode coupling. In [70], the excitation of dark pulses (dark comb) was demonstrated with the aid of mode interactions in normal dispersion microresonators. In addition, linear coupled cavities implemented in [91, 92] allow controlled mode interaction for DKSs generation in the normal dispersion region. In paper D, we used this concept to generate one of the DKSs to exemplify the characterization technique discussed in section 4.4.2.

4.3 DKS combs simulation

For anomalous dispersion, a DKS can be generated by scanning the CW laser from the blue to the red side of the resonance. In general, the comb state goes through a chaotic region since the final state depends on the initial noise state [93]. The soliton states can be controlled in a deterministic manner by careful laser tuning [94] or changing the refractive index of the waveguides thermally [95] which we used in paper D. Figure 4.4 is the Ikeda map simulation of the single DKS and multi-DKS (two solitons) for a 100 GHz repetition rate. The multi-DKS has a spectral modulation of a 10-FSR period.

The DKS microcombs in both temporal and spectral intensity re-

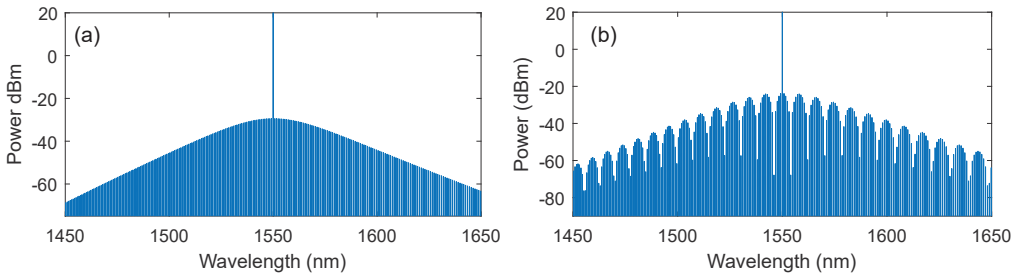

Figure 4.4: Simulated 100 GHz single (a) and multisoliton (b) combs. The comb parameters are as follows: $\alpha = 3$ dB/m, $\beta_2 = -65$ ps^2/km, FSR $= 100$ GHz, $n_g = 2.1$, $\gamma = 1$ W^{-1}m^{-1}, $\delta_0 = 0.028$ rad, $P_{\text{in}} = 20$ dBm, $\theta = 0.0014$.

sponses are hyperbolic secant. Figure 4.5 is the waveform of the single DKS of Fig 4.4(a). The temporal intracavity intensity and phase profiles are in Fig. 4.5(a) and (b). The phase response of the DKS spectrum is approximately constant except at the pump frequency (Fig. 4.5(c)). This pump phase offset is attributed to the field interaction at the coupling region [96] and self-organization in the comb formation process [97]. The differential phase of the spectrum is shown in Fig. 4.5(d). In paper D, we illustrated the stepped heterodyne technique to reconstruct the differential phase.

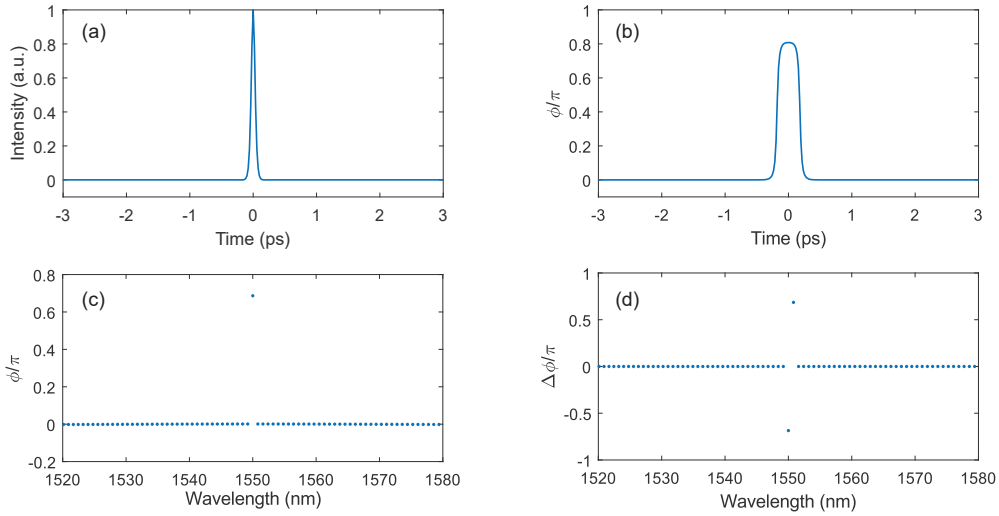

Figure 4.5: Temporal and spectral waveform of the single DKS simulated by the Ikeda map in Fig 4.4(a). (a) Temporal pulse profile. (b) Temporal phase profile. (c) spectral phase of the 100 GHz repetition rate comb modes . (d) Differential phase of the comb modes.

Figure 4.6 shows the waveform of the multi-DKS comb of 4.4(b). It has two intracavity soliton pulses circulating in the cavity at 1 ps apart.

The temporal intensity and phase profiles are shown in Fig 4.6(a) and (b). The phase profile (Fig. 4.6(c) and (d)) shows a π phase transition at the spectral intensity modulation dip. Analyzing these structures in amplitude and phase is crucial for understanding the comb dynamics. However, it represents a challenge for standard characterization techniques as discussed in Paper [C].

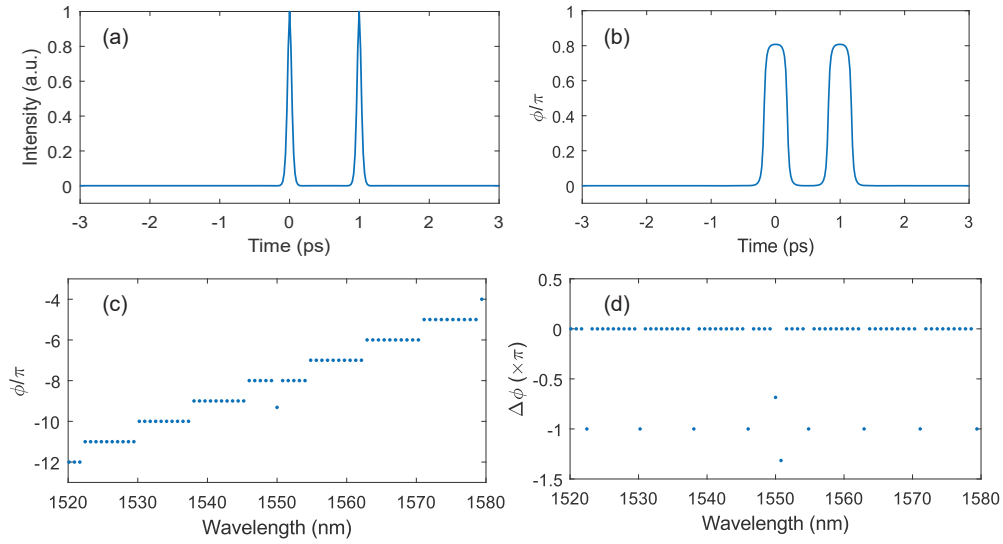

Figure 4.6: Temporal and spectral waveform of the multi-DKS simulated by the Ikeda map in Fig 4.4(b). (a) Temporal pulse profile. (b) Temporal phase profile. (c) spectral phase of the 100 GHz repetition rate comb modes . (d) Differential phase of the comb modes.

4.4 Characterization of frequency combs

The rapid development of ultrafast optics in the past decades has found a myriad of applications. It has led research to focus on the complex spectral characterization and recreates its temporal intensity and phase profile. Indeed, several methods based on optical nonlinearities have been reported such as frequency-resolved optical grating (FROG) [98] and spectral phase interferometry (SPIDER) [99], direct optical spectral phase measurement (DOSPM) [100]. These grating based optical spectrum analyzers have limited frequency resolution. In addition, the autocorrelation technique is also widely adopted for estimating the pulse duration [101]. These nonlinear techniques require high peak power to generate a second harmonic signal. Instead, the complete amplitude and phase characterization of optical pulses based on linear techniques have

been reported in literature. These techniques measure the phase difference between adjacent modes. In [102], the phase difference is inferred from the measured beat note between adjacent spectral modes. As a complex spectrum analyzer, an optical heterodyne technique of beating a reference laser with the spectral modes is illustrated in [103, 104]. This technique is known as stepped-heterodyne technique. In the following section, we provide more insight into this technique and apply to the EO comb. In Paper [C], we applied this technique with electro-optic down-conversion for various comb states. It is also possible to acquire the complex spectrum of comb in a single real-time trace by using a reference comb of slightly different repetition rate [105, 106]. These methods provide internal phase reference and excellent dynamic range. In [107], a reference laser is phase modulated to record a beat note with a low bandwidth receiver.

4.4.1 Stepped heterodyne characterization

Stepped heterodyne is a linear method of complex spectral and temporal measurement of periodic optical signals. The idea lies in beating the signal waveform with a continuous-wave laser that is tuned in a stepped-wise manner across the comb tones as shown in Fig. 4.7(a). The phase of the consecutive lines is embedded in the downconverted radio-frequency beat notes.

For an optical frequency $\omega_{s(ref)}$, phase noise $\phi_{s(ref)}$, and power of the optical carrier $P_{\mu(ref)}$ (reference signal), the complex electric field of the periodic signal under test of period $2\pi/\omega_r$ can be written as:

$$E_{sig.}(t) = \sum_{\mu=-n}^{n} (\sqrt{P_\mu}\exp(j\mu\omega_r t + j\phi_\mu)\exp(j\omega_s t + j\phi_s(t)). \tag{4.10}$$

The complex electric filed of reference signal is:

$$E_{ref}(t) = \sqrt{P_{ref}}\exp(j\omega_{ref} t + j\phi_{ref}(t)). \tag{4.11}$$

The crucial parameter under investigation is the static spectral phase ϕ_μ of the μ^{th} mode number. In the stepped heterodyne technique these two signals are mixed on a square law balanced photodetector. Figure 4.7(c) is the interference pattern acquired from the real time scope for 200 ns of interval. This in turn generates three nontrivial RF heterodyne beat tones (Fig. 4.7(d)).

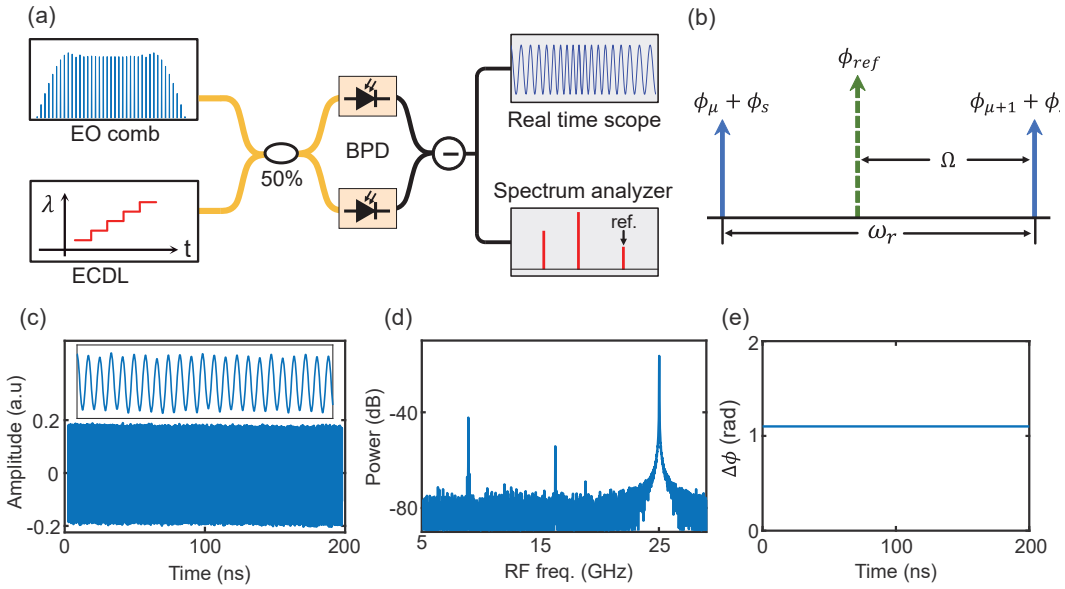

Figure 4.7: Stepped heterodyne optical complex spectrum analyzer.(a) Schematic diagram showing the beating between the EO-comb and reference laser (ECDL). (b) Spectral lines with the corresponding phase. (c) Interference pattern of beat signals and zoom in the inset. (d) RF beat note spectrum. (e) Differential phase of the one pair of the EO-comb lines. ECDL: External cavity diode laser, BPF: Balanced photodiode.

Consider the reference laser is in between comb modes μ and $\mu + 1$ as shown in Fig. 4.7(b). The complex electric field of beat tones can be expressed as [103]

$$\begin{aligned} E_{beat}(t) = &\sqrt{P_{ref}P_{\mu+1}}\exp(j(\Omega t + \phi_{ref}(t) - \phi_s(t) - \phi_{\mu+1})) \\ &+ \sqrt{P_{ref}P_{\mu}}\exp(j((\omega_r - \Omega)t - \phi_{ref}(t) + \phi_s(t) + \phi_{\mu})) \\ &+ \sqrt{P_{net}}\exp(j(\omega_r t + \phi_{net})), \end{aligned} \tag{4.12}$$

with $\Omega \leq \omega_r/2$ denoting detuning of the reference laser from the nearest mode. P_{net} and ϕ_{net} denote accumulate power and phase of beating between adjacent comb modes respectively. The bandwidth limit of the detector is assumed to be equal the repetition rate of the comb f_r. The first two terms correspond to the beating of reference signal with the two nearest comb lines. The beating of adjacent comb lines corresponds to the last term. This beating signal is common for all stepped measurements and independent of the location of the reference laser. Therefore, this signal is used as a reference in the phase difference calculation. These spectra are retrieved applying Fourier transform and digital filters centered at Ω, $\omega_r - \Omega$, and ω_r. The combination of the first two terms results

in $P_{ref}\sqrt{P_{\mu}P_{\mu+1}}\exp(j(\omega_r t + \phi_{\mu} - \phi_{\mu+1}))$ with no phase noise contributions. The product of this signal with the conjugate of the reference signal yields a signal with an argument $\phi_{\mu-1} - \phi_{\mu} - \phi_{net}$ as a function of time Fig. 4.7(e). The differential phase $\Delta\phi_{\mu} = \langle\phi_{\mu-1} - \phi_{\mu} - \phi_{net}\rangle$ is then calculated by taking the average of this signal. The constant phase offset term ϕ_{net} introduces a linear phase in the spectral phase reconstruction. While it shifts the pulse in time, it will not affect in the reconstruction of the pulse shape.

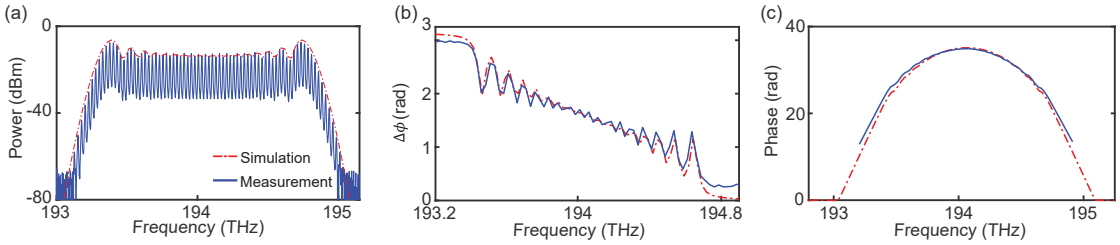

Figure 4.8: Stepped heterodyne complex spectrum analysis of the EO comb (red: simulation and blue: measurement).(a) EO comb spectrum. The modulation depth was set to 14.25 in the simulation. (b) Differential phase profile. (c) Reconstruction of the spectral phase response.

Figure 4.8 shows the stepped heterodyne technique applied to an EO comb and validated with the simulation. The EO-comb consists of cascaded modulators in a sequence as PM-PM-IM.

4.4.2 Microcomb characterization

Stable microcombs can be generated in numerous shapes. The microcombs can have various coherent states and complex pulse profiles [22]. It is important to measure the phase of comb lines to understand the comb dynamics and full-field characterization. However, measuring the phase for broadband range encounters several challenges in the context of microcombs. In the following, we discuss potential challenges and how we mitigated those issues (more detail in Paper [C]).

Intensity autocorrelation is commonly used to measure the phase of the comb lines. In this technique, the relative phase of comb lines is iterated via spatial light modulator (pulse shaper) to obtain a maximum amplitude modulation in the autocorrelation response. This is the idea of optimizing the spectral phase of a pulse until the shortest (transform-limited) pulse is realized. Then the phase of the comb lines is inferred from the reverse of the phase applied to the pulse shaper. In [31], a

conventional pulse characterization technique frequency-resolved optical grating (FROG) was implemented to demonstrate a transform-limited optical pulses of a single-soliton 35 GHz comb. For an integrated platform, it is challenging to implement FROG due to the high repetition rate and the fact that the pulse waveforms of the microcombs have very low energy. In addition, there are plenty of microcombs that are not transform-limited, hence further reducing the peak intensity, such as, e.g., dark combs [70], and coupled cavity combs [92, 108], and soliton crystals [109]. However, the intensity autocorrelation technique allows measuring phases of the low power comb lines and offers high dynamic range. This technique was adopted to fully characterize distinct microcombs states in [32, 70]. The autocorrelation measurement is a nonlinear process requiring a high signal power to induce sufficient second harmonic yield. Therefore, it needs an optical amplifier to boost the signal power. However, gain bandwidth of the amplifier or the bandwidth of the pulse shaper therefore limits the measurement range. In addition, this method is time consuming due to the line-by-line phase iteration of the comb modes. In [110], a concept of electric field cross correlation [111] in the microcomb phase measurement is reported. In this method, a calibrated reference comb is heterodyned with the comb under test. It shares the same technical principle as dual comb spectroscopy, allowing reconstruction of the phase in a single-shot measurement. Nonetheless, the necessity of reference comb phase calibration ultimately leads to the aforementioned limitations i.e. limited bandwidth of the optical instrumentation.

In contrast, the stepped heterodyne technique described in section 4.4.1 does not require reference laser calibration. It measures the differential phase comparing the phase of photodetected beatnotes which is independent of the phase noise of the seed laser and reference laser. The beatnotes power is proportional to the product of the reference laser and comb line power. This in turn provides high sensitivity. This technique has been implemented to characterize various periodic signals. In [103], optical pulses and passively mode-locked lasers were characterized for both amplitude and phase in the spectral and temporal domain. An electronic down conversion with an aid of a local oscillator of the detected beatnotes allows characterizing a ~ 40 GHz modelocked laser [112]. However, in the realm of microcombs repetition rates can go beyond the state of the art electronics detection range. In paper [D], we implemented the stepped heterodyne technique in the context of micro-

combs. The large repetition rate was made accessible by electro-optic downconversion of the comb lines. For this, we used a phase modulator (PM) to bring the comb lines closer in the form of sidebands. The sideband carries the phase information of the comb line with a irrelevant constant offset.

Figure 4.9 is the spectral and temporal characterization of the multisoliton comb. The microresonator was pumped with an on-chip power of 20.5 dBm at 1557.179 nm wavelength. The electro-optic phase modulator was driven by a 24.58 GHz RF clock. This in turn generates second-order sidebands 1.575 GHz apart from the adjacent comb lines. We used a stepped heterodyne technique discussed in section 4.4.1 to retrieve the differential phase 4.9(b). The spectral phase profile in Fig. 4.9(c) was reconstructed by integrating the differential phase. This phase profile is identical to the phase shown in Fig. 4.6(c). The spectral amplitude and phase profile was used to reconstruct the temporal pulse profile (Fig. 4.9(d)).

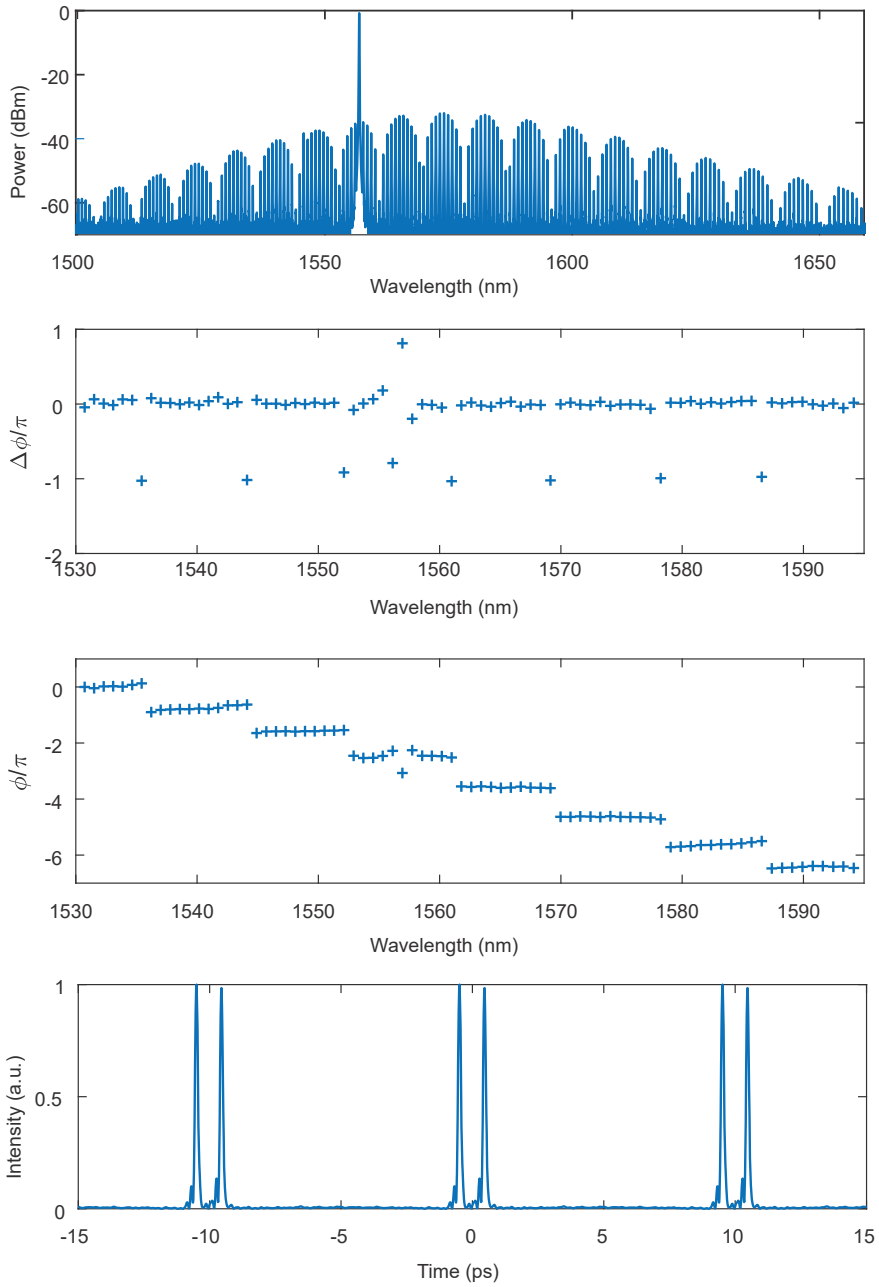

Figure 4.9: Spectral and temporal characterization of the multisoliton comb. (a) Spectrum of the microcomb of a repetition rate 99.895 GHz. (b) Differential phase measurement of the comb. (c) Reconstruction of the phase. (d) Temporal reconstruction of the pulse. The pulse repetition rate is 10.011 ps and the separation between two pulses is 0.951 ps.

Chapter 5

Future outlook

This thesis has focused on the interferometric modality of characterizing photonic devices. The tuning laser that probes the sample was calibrated with a self-referenced frequency comb. It enabled ultra-wide bandwidth and a large dynamic measurement range of an SWI system. The soliton dynamics in a microcavity with temporal and spectral distributions were illustrated. There are numerous fascinating follow-up research question related to the work presented in this thesis. Here, I highlight some areas that in my opinion are worth to be explored.

- Papers A-C illustrated the fiber laser self-referenced comb calibrated swept-wavelength interferometry. The equidistant frequency lines from the comb provide thousands of precise references in the laser calibration. It would be interesting to replace the fiber comb with the microcomb. Microcombs of < 20 GHz can be generated and the gap can be filled by generating subcombs with an elector-optic modulation. The RF frequency can be set such that spacing between the lines is even throughout the spectral range.

- Paper D demonstrated the stepped heterodyne technique to reconstruct the differential phase of the microcombs. This involves stepping the laser with the repetition rate of the comb. It would be interesting to implement this illustration with a multi-heterodyne detection technique. It needs another microcomb with a slightly different repetition rate. This enables imaging of comb dynamics in the cavity.

Chapter 6

Summary of papers

Paper A

Frequency-comb-calibrated swept-wavelength interferometry,
Optics Express, 29, 15, 24363-24372, 2021.

Here, we demonstrate the non-destructive broadband characterization in amplitude and phase of ultra-low-loss microresonators and spiral waveguides. The device under test is arranged in an interferometric configuration. The swept laser is calibrated using a self-referenced fiber laser comb to map the time axis of the acquired interference pattern into frequency axis. The measured phase distribution of the resonances enables distinguishing intrinsic loss from coupling loss. The parametric fitting of the resonances is done based on the coupled mode theory.

My contributions: I conducted the measurements and simulations, I wrote the paper with support from co-authors. I presented the work at CLEO EU 2021.

Paper B

Spectral Interferometry with Frequency Combs,
Micromachines, 13, 4, 614, 2022.

In this work, we review the state of the art in linear interferometric techniques using a laser frequency comb source. We present different techniques; Fourier-transform spectroscopy, linear spectral

interferometry, and swept wavelength interferometry and highlight some applications.

My contributions: I wrote sections 3.3, 3.4, 4.3, and 4.4 in the manuscript.

Paper C

Differential phase reconstruction of microcombs,
Submitted 2022.

In this paper, we show a linear heterodyne technique to characterize the single and coupled cavity microcombs. This technique enables measuring broadband differential phase between consecutive comb lines with unprecedented bandwidth and power sensitivity. The phase difference measurement of high repetition rate comb is assisted by electro-optic downconversion.

My contributions: I conducted the lab experiments and simulations with co-authors. I wrote the manuscript with co-authors and I presented the preliminary results at CLEO 2022.

References

[1] M. Giunta, M. Fischer, W. Hänsel, T. Steinmetz, M. Lessing, S. Holzberger, C. Cleff, T. W. Hänsch, M. Mei, and R. Holzwarth, "20 years and 20 decimal digits: A journey with optical frequency combs," *IEEE Photonics Technology Letters*, vol. 31, no. 23, pp. 1898–1901, 2019.

[2] T. W. Hänsch, "Nobel lecture: passion for precision," *Reviews of Modern Physics*, vol. 78, no. 4, p. 1297, 2006.

[3] D. J. Jones, S. A. Diddams, J. K. Ranka, A. Stentz, R. S. Windeler, J. L. Hall, and S. T. Cundiff, "Carrier-envelope phase control of femtosecond mode-locked lasers and direct optical frequency synthesis," *Science*, vol. 288, no. 5466, pp. 635–639, 2000.

[4] R. Holzwarth, T. Udem, T. W. Hänsch, J. Knight, W. Wadsworth, and P. S. J. Russell, "Optical frequency synthesizer for precision spectroscopy," *Physical review letters*, vol. 85, no. 11, p. 2264, 2000.

[5] P. Del'Haye, A. Schliesser, O. Arcizet, T. Wilken, R. Holzwarth, and T. J. Kippenberg, "Optical frequency comb generation from a monolithic microresonator," *Nature*, vol. 450, no. 7173, pp. 1214–1217, 2007.

[6] J. S. Levy, A. Gondarenko, M. A. Foster, A. C. Turner-Foster, A. L. Gaeta, and M. Lipson, "CMOS-compatible multiple-wavelength oscillator for on-chip optical interconnects," *Nature Photonics*, vol. 4, no. 1, pp. 37–40, 2010.

[7] R. Soref and J. Larenzo, "All-silicon active and passive guided-wave components for λ= 1.3 and 1.6 μm," *IEEE Journal of Quantum Electronics*, vol. 22, no. 6, pp. 873–879, 1986.

[8] V. R. Almeida, R. R. Panepucci, and M. Lipson, "Nanotaper for compact mode conversion," *Optics Letters*, vol. 28, no. 15, pp. 1302–1304, 2003.

[9] Q. Xu, B. Schmidt, S. Pradhan, and M. Lipson, "Micrometre-scale silicon electro-optic modulator," *Nature*, vol. 435, no. 7040, pp. 325–327, 2005.

[10] D. Melati, A. Alippi, and A. Melloni, "Waveguide-based technique for wafer-level measurement of phase and group effective refractive indices," *Journal of Lightwave Technology*, vol. 34, no. 4, pp. 1293–1299, 2015.

[11] F. Morichetti, A. Canciamilla, C. Ferrari, M. Torregiani, A. Melloni, and M. Martinelli, "Roughness induced backscattering in optical silicon waveguides," *Physical Review Letters*, vol. 104, no. 3, p. 033902, 2010.

[12] P. Del'Haye, O. Arcizet, M. L. Gorodetsky, R. Holzwarth, and T. J. Kippenberg, "Frequency comb assisted diode laser spectroscopy for measurement of microcavity dispersion," *Nature Photonics*, vol. 3, no. 9, pp. 529–533, 2009.

[13] H. Schnatz, B. Lipphardt, J. Helmcke, F. Riehle, and G. Zinner, "First phase-coherent frequency measurement of visible radiation," *Physical Review Letters*, vol. 76, no. 1, p. 18, 1996.

[14] P. F. Moulton, "Spectroscopic and laser characteristics of Ti: Al_2O_3 3," *JOSA B*, vol. 3, no. 1, pp. 125–133, 1986.

[15] D. E. Spence, P. N. Kean, and W. Sibbett, "60-fsec pulse generation from a self-mode-locked ti: sapphire laser," *Optics Letters*, vol. 16, no. 1, pp. 42–44, 1991.

[16] T. Udem, R. Holzwarth, and T. W. Hänsch, "Optical frequency metrology," *Nature*, vol. 416, no. 6877, pp. 233–237, 2002.

[17] T. Fortier and E. Baumann, "20 years of developments in optical frequency comb technology and applications," *Communications Physics*, vol. 2, no. 1, pp. 1–16, 2019.

[18] S. A. Diddams, K. Vahala, and T. Udem, "Optical frequency combs: Coherently uniting the electromagnetic spectrum," *Science*, vol. 369, no. 6501, p. eaay3676, 2020.

[19] H. Murata, A. Morimoto, T. Kobayashi, and S. Yamamoto, "Optical pulse generation by electrooptic-modulation method and its application to integrated ultrashort pulse generators," *IEEE Journal of Selected Topics in Quantum Electronics*, vol. 6, no. 6, pp. 1325–1331, 2000.

[20] A. J. Metcalf, V. Torres-Company, D. E. Leaird, and A. M. Weiner, "High-power broadly tunable electrooptic frequency comb generator," *IEEE Journal of Selected Topics in Quantum Electronics*, vol. 19, no. 6, pp. 231–236, 2013.

[21] V. Torres-Company and A. M. Weiner, "Optical frequency comb technology for ultra-broadband radio-frequency photonics," *Laser & Photonics Reviews*, vol. 8, no. 3, pp. 368–393, 2014.

[22] A. Pasquazi, M. Peccianti, L. Razzari, D. J. Moss, S. Coen, M. Erkintalo, Y. K. Chembo, T. Hansson, S. Wabnitz, P. Del'Haye *et al.*, "Micro-combs: A novel generation of optical sources," *Physics Reports*, vol. 729, pp. 1–81, 2018.

[23] E. Cartlidge, "Combs of light on a chip," *Optics and Photonics News*, vol. 32, no. 1, pp. 26–33, 2021.

[24] Q.-F. Yang, M.-G. Suh, K. Y. Yang, X. Yi, and K. J. Vahala, "Microresonator soliton dual-comb spectroscopy," in *CLEO: Science and Innovations*. Optical Society of America, 2017, pp. SM4D–4.

[25] P. Marin-Palomo, J. N. Kemal, M. Karpov, A. Kordts, J. Pfeifle, M. H. Pfeiffer, P. Trocha, S. Wolf, V. Brasch, M. H. Anderson *et al.*, "Microresonator-based solitons for massively parallel coherent optical communications," *Nature*, vol. 546, no. 7657, pp. 274–279, 2017.

[26] A. Fülöp, M. Mazur, A. Lorences-Riesgo, Ó. B. Helgason, P.-H. Wang, Y. Xuan, D. E. Leaird, M. Qi, P. A. Andrekson, A. M. Weiner *et al.*, "High-order coherent communications using mode-locked dark-pulse Kerr combs from microresonators," *Nature Communications*, vol. 9, no. 1, pp. 1–8, 2018.

[27] X. Xu, J. Wu, T. G. Nguyen, M. Shoeiby, S. T. Chu, B. E. Little, R. Morandotti, A. Mitchell, and D. J. Moss, "Advanced RF and microwave functions based on an integrated optical frequency comb source," *Optics Express*, vol. 26, no. 3, pp. 2569–2583, 2018.

[28] D. T. Spencer, T. Drake, T. C. Briles, J. Stone, L. C. Sinclair, C. Fredrick, Q. Li, D. Westly, B. R. Ilic, A. Bluestone *et al.*, "An optical-frequency synthesizer using integrated photonics," *Nature*, vol. 557, no. 7703, pp. 81–85, 2018.

[29] T. Kippenberg, S. Spillane, and K. Vahala, "Kerr-nonlinearity optical parametric oscillation in an ultrahigh-q toroid microcavity," *Physical Review Letters*, vol. 93, no. 8, p. 083904, 2004.

[30] P. Del'Haye, O. Arcizet, A. Schliesser, R. Holzwarth, and T. J. Kippenberg, "Full stabilization of a microresonator-based optical frequency comb," *Physical Review Letters*, vol. 101, no. 5, p. 053903, 2008.

[31] T. Herr, V. Brasch, J. D. Jost, C. Y. Wang, N. M. Kondratiev, M. L. Gorodetsky, and T. J. Kippenberg, "Temporal solitons in optical microresonators," *Nature Photonics*, vol. 8, no. 2, pp. 145–152, 2014.

[32] P. Del'Haye, A. Coillet, W. Loh, K. Beha, S. B. Papp, and S. A. Diddams, "Phase steps and resonator detuning measurements in microresonator frequency combs," *Nature Communications*, vol. 6, no. 1, pp. 1–9, 2015.

[33] S. T. Cundiff and A. M. Weiner, "Optical arbitrary waveform generation," *Nature Photonics*, vol. 4, no. 11, pp. 760–766, 2010.

[34] B. L. Danielson, "Optical time-domain reflectometer specifications and performance testing," *Applied Optics*, vol. 24, no. 15, pp. 2313–2322, 1985.

[35] B. R. Masters, "Early development of optical low-coherence reflectometry and some recent biomedical applications," *Journal of Biomedical Optics*, vol. 4, no. 2, pp. 236–247, 1999.

[36] R. C. Youngquist, S. Carr, and D. E. Davies, "Optical coherence-domain reflectometry: a new optical evaluation technique," *Optics Letters*, vol. 12, no. 3, pp. 158–160, 1987.

[37] D. Huang, E. A. Swanson, C. P. Lin, J. S. Schuman, W. G. Stinson, W. Chang, M. R. Hee, T. Flotte, K. Gregory, C. A. Puliafito *et al.*, "Optical coherence tomography," *Science*, vol. 254, no. 5035, pp. 1178–1181, 1991.

[38] B. J. Soller, D. K. Gifford, M. S. Wolfe, and M. E. Froggatt, "High resolution optical frequency domain reflectometry for characterization of components and assemblies," *Optics Express*, vol. 13, no. 2, pp. 666–674, 2005.

[39] P. Chaisakul, D. Marris-Morini, J. Frigerio, D. Chrastina, M.-S. Rouifed, S. Cecchi, P. Crozat, G. Isella, and L. Vivien, "Integrated germanium optical interconnects on silicon substrates," *Nature Photonics*, vol. 8, no. 6, pp. 482–488, 2014.

[40] S.-H. Yun, G. J. Tearney, J. F. de Boer, N. Iftimia, and B. E. Bouma, "High-speed optical frequency-domain imaging," *Optics Express*, vol. 11, no. 22, pp. 2953–2963, 2003.

[41] M. Froggatt and J. Moore, "High-spatial-resolution distributed strain measurement in optical fiber with Rayleigh scatter," *Applied Optics*, vol. 37, no. 10, pp. 1735–1740, 1998.

[42] W. Eickhoff and R. Ulrich, "Optical frequency domain reflectometry in single-mode fiber," *Applied Physics Letters*, vol. 39, no. 9, pp. 693–695, 1981.

[43] S. Personick, "Photon probe—an optical-fiber time-domain reflectometer," *The bell system technical journal*, vol. 56, no. 3, pp. 355–366, 1977.

[44] M. Barnoski, M. Rourke, S. Jensen, and R. Melville, "Optical time domain reflectometer," *Applied Optics*, vol. 16, no. 9, pp. 2375–2379, 1977.

[45] E. D. Moore, "Advances in swept-wavelength interferometry for precision measurements," Ph.D. dissertation, University of Colorado at Boulder, 2011.

[46] P. A. Roos, R. R. Reibel, T. Berg, B. Kaylor, Z. W. Barber, and W. R. Babbitt, "Ultrabroadband optical chirp linearization for precision metrology applications," *Optics Letter*, vol. 34, no. 23, pp. 3692–3694, 2009.

[47] K. Iiyama, L.-T. Wang, and K.-I. Hayashi, "Linearizing optical frequency-sweep of a laser diode for FMCW reflectometry," *Journal of Lightwave Technology*, vol. 14, no. 2, pp. 173–178, 1996.

[48] U. Glombitza and E. Brinkmeyer, "Coherent frequency-domain reflectometry for characterization of single-mode integrated-optical waveguides," *Journal of Lightwave technology*, vol. 11, no. 8, pp. 1377–1384, 1993.

[49] E. D. Moore and R. R. McLeod, "Correction of sampling errors due to laser tuning rate fluctuations in swept-wavelength interferometry," *Optics Express*, vol. 16, no. 17, pp. 13 139–13 149, 2008.

[50] S. Fujii and T. Tanabe, "Dispersion engineering and measurement of whispering gallery mode microresonator for kerr frequency comb generation," *Nanophotonics*, vol. 9, no. 5, pp. 1087–1104, 2020.

[51] E. Baumann, F. R. Giorgetta, I. Coddington, L. C. Sinclair, K. Knabe, W. C. Swann, and N. R. Newbury, "Comb-calibrated frequency-modulated continuous-wave ladar for absolute distance measurements," *Optics Letters*, vol. 38, no. 12, pp. 2026–2028, 2013.

[52] W. Yu, P. Pfeiffer, A. Morsali, J. Yang, and J. Fontaine, "Comb-calibrated frequency sweeping interferometry for absolute distance and vibration measurement," *Optics Letters*, vol. 44, no. 20, pp. 5069–5072, 2019.

[53] E. Baumann, F. R. Giorgetta, J.-D. Deschênes, W. C. Swann, I. Coddington, and N. R. Newbury, "Comb-calibrated laser ranging for three-dimensional surface profiling with micrometer-level precision at a distance," *Optics Express*, vol. 22, no. 21, pp. 24 914–24 928, 2014.

[54] J. Liu, V. Brasch, M. H. Pfeiffer, A. Kordts, A. N. Kamel, H. Guo, M. Geiselmann, and T. J. Kippenberg, "Frequency-comb-assisted broadband precision spectroscopy with cascaded diode lasers," *Optics Letters*, vol. 41, no. 13, pp. 3134–3137, 2016.

[55] R. MacDonald, "Frequency domain optical reflectometer," *Applied Optics*, vol. 20, no. 10, pp. 1840–1844, 1981.

[56] J. Von Der Weid, R. Passy, G. Mussi, and N. Gisin, "On the characterization of optical fiber network components with optical frequency domain reflectometry," *Journal of Lightwave Technology*, vol. 15, no. 7, pp. 1131–1141, 1997.

[57] M. Badar, P. Lu, M. Buric, and P. Ohodnicki Jr, "Integrated auxiliary interferometer for self-correction of nonlinear tuning in optical frequency domain reflectometry," *Journal of Lightwave Technology*, vol. 38, no. 21, pp. 6097–6103, 2020.

[58] K. Twayana, Z. Ye, Ó. B. Helgason, K. Vijayan, M. Karlsson *et al.*, "Frequency-comb-calibrated swept-wavelength interferometry," *Optics Express*, vol. 29, no. 15, pp. 24 363–24 372, 2021.

[59] J. F. Bauters, M. J. Heck, D. D. John, J. S. Barton, C. M. Bruinink, A. Leinse, R. G. Heideman, D. J. Blumenthal, and J. E. Bowers, "Planar waveguides with less than 0.1 dB/m propagation loss fabricated with wafer bonding," *Optics Express*, vol. 19, no. 24, pp. 24 090–24 101, 2011.

[60] L. A. Bru, D. Pastor, and P. Muñoz, "Integrated optical frequency domain reflectometry device for characterization of complex integrated devices," *Optics Express*, vol. 26, no. 23, pp. 30 000–30 008, 2018.

[61] X. Zhang, Y. Yin, X. Yin, Y. Wen, X. Zhang, X. Liu, and H. Lv, "Characterizing microring resonators using optical frequency domain reflectometry," *Optics Letters*, vol. 46, no. 10, pp. 2400–2403, 2021.

[62] J.-P. von der Weid, R. Passy, and N. Gisin, "Mid-range coherent optical frequency domain reflectometry with a DFB laser diode coupled to an external cavity," *Journal of Lightwave Technology*, vol. 13, no. 5, pp. 954–960, 1995.

[63] Z. Ye, P. Zhao, K. Twayana, M. Karlsson, P. A. Andrekson, and V. Torres-Company, "Ultralow-loss meter-long dispersion-engineered silicon nitride waveguides," in *2021 Conference on Lasers and Electro-Optics (CLEO)*. IEEE, 2021, pp. 1–2.

[64] Z. Ye, P. Zhao, K. Twayana, M. Karlsson, V. Torres-Company, and P. A. Andrekson, "Overcoming the quantum limit of optical amplification in monolithic waveguides," *Science Advances*, vol. 7, no. 38, p. eabi8150, 2021.

[65] Z. Ye, "Ultralow-loss silicon nitride waveguides for nonlinear optics," Ph.D. dissertation, Chalmers Tekniska Hogskola (Sweden), 2021.

[66] T. Herr, V. Brasch, J. Jost, I. Mirgorodskiy, G. Lihachev, M. Gorodetsky, and T. Kippenberg, "Mode spectrum and temporal soliton formation in optical microresonators," *Physical Review Letters*, vol. 113, no. 12, p. 123901, 2014.

[67] W. Bogaerts, P. De Heyn, T. Van Vaerenbergh, K. De Vos, S. Kumar Selvaraja, T. Claes, P. Dumon, P. Bienstman, D. Van Thourhout, and R. Baets, "Silicon microring resonators," *Laser & Photonics Reviews*, vol. 6, no. 1, pp. 47–73, 2012.

[68] J. Niehusmann, A. Vörckel, P. H. Bolivar, T. Wahlbrink, W. Henschel, and H. Kurz, "Ultrahigh-quality-factor silicon-on-insulator microring resonator," *Optics Letters*, vol. 29, no. 24, pp. 2861–2863, 2004.

[69] W. McKinnon, D.-X. Xu, C. Storey, E. Post, A. Densmore, A. Delâge, P. Waldron, J. Schmid, and S. Janz, "Extracting coupling and loss coefficients from a ring resonator," *Optics Express*, vol. 17, no. 21, pp. 18 971–18 982, 2009.

[70] X. Xue, Y. Xuan, Y. Liu, P.-H. Wang, S. Chen, J. Wang, D. E. Leaird, M. Qi, and A. M. Weiner, "Mode-locked dark pulse kerr combs in normal-dispersion microresonators," *Nature Photonics*, vol. 9, no. 9, pp. 594–600, 2015.

[71] J. E. Heebner, V. Wong, A. Schweinsberg, R. W. Boyd, and D. J. Jackson, "Optical transmission characteristics of fiber ring resonators," *IEEE Journal of Quantum Electronics*, vol. 40, no. 6, pp. 726–730, 2004.

[72] Y. Xuan, Y. Liu, L. T. Varghese, A. J. Metcalf, X. Xue, P.-H. Wang, K. Han, J. A. Jaramillo-Villegas, A. Al Noman, C. Wang *et al.*, "High-Q silicon nitride microresonators exhibiting low-power frequency comb initiation," *Optica*, vol. 3, no. 11, pp. 1171–1180, 2016.

[73] A. Li, T. Van Vaerenbergh, P. De Heyn, P. Bienstman, and W. Bogaerts, "Backscattering in silicon microring resonators: a quantitative analysis," *Laser & Photonics Reviews*, vol. 10, no. 3, pp. 420–431, 2016.

[74] M. H. Pfeiffer, J. Liu, A. S. Raja, T. Morais, B. Ghadiani, and T. J. Kippenberg, "Ultra-smooth silicon nitride waveguides based

on the damascene reflow process: fabrication and loss origins," *Optica*, vol. 5, no. 7, pp. 884–892, 2018.

[75] K. Wu and A. W. Poon, "Stress-released Si_3N_4 fabrication process for dispersion-engineered integrated silicon photonics," *Optics Express*, vol. 28, no. 12, pp. 17 708–17 722, 2020.

[76] M. L. Gorodetsky, A. D. Pryamikov, and V. S. Ilchenko, "Rayleigh scattering in high-Q microspheres," *JOSA B*, vol. 17, no. 6, pp. 1051–1057, 2000.

[77] G. Tittelbach, B. Richter, and W. Karthe, "Comparison of three transmission methods for integrated optical waveguide propagation loss measurement," *Pure and Applied Optics: Journal of the European Optical Society Part A*, vol. 2, no. 6, p. 683, 1993.

[78] J. F. Bauters, M. J. Heck, D. John, D. Dai, M.-C. Tien, J. S. Barton, A. Leinse, R. G. Heideman, D. J. Blumenthal, and J. E. Bowers, "Ultra-low-loss high-aspect-ratio si 3 n 4 waveguides," *Optics Express*, vol. 19, no. 4, pp. 3163–3174, 2011.

[79] M. Melchiorri, N. Daldosso, F. Sbrana, L. Pavesi, G. Pucker, C. Kompocholis, P. Bellutti, and A. Lui, "Propagation losses of silicon nitride waveguides in the near-infrared range," *Applied Physics Letters*, vol. 86, no. 12, p. 121111, 2005.

[80] R. Adar, M. Serbin, and V. Mizrahi, "Less than 1 dB per meter propagation loss of silica waveguides measured using a ring resonator," *Journal of Lightwave Technology*, vol. 12, no. 8, pp. 1369–1372, 1994.

[81] P. Rabiei, W. H. Steier, C. Zhang, and L. R. Dalton, "Polymer micro-ring filters and modulators," *Journal of Lightwave Technology*, vol. 20, no. 11, p. 1968, 2002.

[82] S. Spillane, T. Kippenberg, O. Painter, and K. Vahala, "Ideality in a fiber-taper-coupled microresonator system for application to cavity quantum electrodynamics," *Physical Review Letters*, vol. 91, no. 4, p. 043902, 2003.

[83] V. Brasch, M. Geiselmann, T. Herr, G. Lihachev, M. H. Pfeiffer, M. L. Gorodetsky, and T. J. Kippenberg, "Photonic chip–based optical frequency comb using soliton cherenkov radiation," *Science*, vol. 351, no. 6271, pp. 357–360, 2016.

[84] M. H. Pfeiffer, C. Herkommer, J. Liu, H. Guo, M. Karpov, E. Lucas, M. Zervas, and T. J. Kippenberg, "Octave-spanning dissipative kerr soliton frequency combs in Si_3N_4 microresonators," *Optica*, vol. 4, no. 7, pp. 684–691, 2017.

[85] F. Ferdous, H. Miao, D. E. Leaird, K. Srinivasan, J. Wang, L. Chen, L. T. Varghese, and A. M. Weiner, "Spectral line-by-line pulse shaping of on-chip microresonator frequency combs," *Nature Photonics*, vol. 5, no. 12, pp. 770–776, 2011.

[86] C. R. Pollock and M. Lipson, *Integrated photonics*. Springer, 2003, vol. 20, no. 25.

[87] G. P. Agrawal, "Nonlinear fiber optics," in *Nonlinear Science at the Dawn of the 21st Century*. Springer, 2000, pp. 195–211.

[88] K. Ikeda, "Multiple-valued stationary state and its instability of the transmitted light by a ring cavity system," *Optics Communications*, vol. 30, no. 2, pp. 257–261, 1979.

[89] L. A. Lugiato and R. Lefever, "Spatial dissipative structures in passive optical systems," *Physical Review Letters*, vol. 58, no. 21, p. 2209, 1987.

[90] D. Castelló-Lurbe, E. Silvestre *et al.*, "Comparative analysis of spectral coherence in microresonator frequency combs," *Optics Express*, vol. 22, no. 4, pp. 4678–4691, 2014.

[91] X. Xue, Y. Xuan, P.-H. Wang, Y. Liu, D. E. Leaird, M. Qi, and A. M. Weiner, "Normal-dispersion microcombs enabled by controllable mode interactions," *Laser & Photonics Reviews*, vol. 9, no. 4, pp. L23–L28, 2015.

[92] Ó. B. Helgason, F. R. Arteaga-Sierra, Z. Ye, K. Twayana, P. A. Andrekson, M. Karlsson, J. Schröder, and V. Torres-Company, "Dissipative solitons in photonic molecules," *Nature Photonics*, vol. 15, no. 4, pp. 305–310, 2021.

[93] S. Coen and M. Erkintalo, "Universal scaling laws of Kerr frequency combs," *Optics Letters*, vol. 38, no. 11, pp. 1790–1792, 2013.

[94] H. Guo, M. Karpov, E. Lucas, A. Kordts, M. H. Pfeiffer, V. Brasch, G. Lihachev, V. E. Lobanov, M. L. Gorodetsky, and T. J. Kippenberg, "Universal dynamics and deterministic switching of dissipative kerr solitons in optical microresonators," *Nature Physics*, vol. 13, no. 1, pp. 94–102, 2017.

[95] C. Joshi, J. K. Jang, K. Luke, X. Ji, S. A. Miller, A. Klenner, Y. Okawachi, M. Lipson, and A. L. Gaeta, "Thermally controlled comb generation and soliton modelocking in microresonators," *Optics Letters*, vol. 41, no. 11, pp. 2565–2568, 2016.

[96] P.-H. Wang, J. A. Jaramillo-Villegas, Y. Xuan, X. Xue, C. Bao, D. E. Leaird, M. Qi, and A. M. Weiner, "Intracavity characterization of micro-comb generation in the single-soliton regime," *Optics Express*, vol. 24, no. 10, pp. 10 890–10 897, 2016.

[97] Y. H. Wen, M. R. Lamont, S. H. Strogatz, and A. L. Gaeta, "Self-organization in kerr-cavity-soliton formation in parametric frequency combs," *Physical Review A*, vol. 94, no. 6, p. 063843, 2016.

[98] D. J. Kane and R. Trebino, "Characterization of arbitrary femtosecond pulses using frequency-resolved optical gating," *IEEE Journal of Quantum Electronics*, vol. 29, no. 2, pp. 571–579, 1993.

[99] C. Iaconis and I. A. Walmsley, "Spectral phase interferometry for direct electric-field reconstruction of ultrashort optical pulses," *Optics Letters*, vol. 23, no. 10, pp. 792–794, 1998.

[100] K. Chu, J. Heritage, R. Grant, K. Liu, A. Dienes, W. White, and A. Sullivan, "Direct measurement of the spectral phase of femtosecond pulses," *Optics Letters*, vol. 20, no. 8, pp. 904–906, 1995.

[101] J. Armstrong, "Measurement of picosecond laser pulse widths," *Applied Physics Letters*, vol. 10, no. 1, pp. 16–18, 1967.

[102] P. Kockaert, M. Peeters, S. Coen, P. Emplit, M. Haelterman, and O. Deparis, "Simple amplitude and phase measuring technique for ultrahigh-repetition-rate lasers," *IEEE Photonics Technology Letters*, vol. 12, no. 2, pp. 187–189, 2000.

[103] D. Reid, S. Murdoch, and L. Barry, "Stepped-heterodyne optical complex spectrum analyzer." *Optics Express*, vol. 18, no. 19, pp. 19 724–19 731, 2010.

[104] M. Korti, T. Habruseva, S. Slepneva, K. Merghem, G. Huyet, Y. Gottesman, A. Ramdane, B.-E. Benkelfat, and O. Seddiki, "Fast-recovery of the amplitude and phase of short optical pulses using a frequency-swept source based heterodyne measurement," *IEEE Photonics Journal*, vol. 10, no. 3, pp. 1–7, 2018.

[105] J. Davila-Rodriguez, M. Bagnell, C. Williams, and P. J. Delfyett, "Multiheterodyne detection for spectral compression and downconversion of arbitrary periodic optical signals," *Journal of Lightwave Technology*, vol. 29, no. 20, pp. 3091–3098, 2011.

[106] T. Butler, B. Tykalewicz, D. Goulding, B. Kelleher, G. Huyet, and S. Hegarty, "Reconstruction of dynamical pulse trains via time-resolved multiheterodyne detection," *Optics Express*, vol. 21, no. 24, pp. 29 109–29 119, 2013.

[107] B. Szafraniec and D. M. Baney, "Swept coherent spectrum analysis of the complex optical field," in *Proceedings of the Lightwave Technologies in Instrumentation and Measurement Conference, 2004.* IEEE, 2004, pp. 68–72.

[108] A. Tikan, J. Riemensberger, K. Komagata, S. Hönl, M. Churaev, C. Skehan, H. Guo, R. N. Wang, J. Liu, P. Seidler *et al.*, "Emergent nonlinear phenomena in a driven dissipative photonic dimer," *Nature Physics*, vol. 17, no. 5, pp. 604–610, 2021.

[109] D. C. Cole, E. S. Lamb, P. Del'Haye, S. A. Diddams, and S. B. Papp, "Soliton crystals in kerr resonators," *Nature Photonics*, vol. 11, no. 10, pp. 671–676, 2017.

[110] Z. Kong, C. Bao, O. E. Sandoval, B. Liu, C. Wang, J. A. Jaramillo-Villegas, M. Qi, and A. M. Weiner, "Characterizing pump line phase offset of a single-soliton kerr comb by dual comb interferometry," *Optics Letters*, vol. 44, no. 6, pp. 1460–1463, 2019.

[111] F. Ferdous, D. E. Leaird, C.-B. Huang, and A. Weiner, "Dual-comb electric-field cross-correlation technique for optical arbitrary waveform characterization," *Optics Letters*, vol. 34, no. 24, pp. 3875–3877, 2009.

[112] S. G. Murdoch, R. T. Watts, Y. Xu, R. Maldonado-Basilio, J. Parra-Cetina, S. Latkowski, P. Landais, and L. P. Barry, "Spectral amplitude and phase measurement of a 40 GHz free-running

quantum-dash modelocked laser diode," *Optics Express*, vol. 19, no. 14, pp. 13 628–13 635, 2011.